Radiation Measurements 130 (2020) 106211

Contents lists available at ScienceDirect

Radiation Measurements

journal homepage: http://www.elsevier.com/locate/radmeas

Medipix detectors in radiation therapy for advanced quality-assurance

Anatoly Rosenfeld [a,*], Saree Alnaghy [a], Marco Petasecca [a], Dean Cutajar [a], Michael Lerch [a], Stanislav Pospisil [b], Valentina Giacometti [c], Reinhard Schulte [d], Valeria Rosso [e], Matthias Würl [f], Carlos Granja [g], Mária Martišíková [h,i,j], Katia Parodi [f]

[a] Center for Medical Radiation Physics, University of Wollongong, Wollongong, NSW, Australia
[b] Institute of Experimental and Applied Physics, Czech Technical University in Prague, Prague, Czech Republic
[c] School of Medicine, Dentistry and Biomedical Sciences, Queen's University Belfast, Belfast, UK
[d] School of Medicine, Loma Linda University, Loma Linda, CA, USA
[e] Department of Physics, University of Pisa and INFN Sezione di Pisa, Pisa, Italy
[f] Department of Medical Physics Ludwig-Maximilians-Universität München, Munich, Germany
[g] Advacam, Prague, Czech Republic
[h] German Cancer Research Center, Heidelberg, Germany
[i] Heidelberg Institute for Radiation Oncology, Heidelberg, Germany
[j] National Center for Radiation Research in Oncology, Heidelberg, Germany

ARTICLE INFO

Keywords:
Medipix
Quality assurance
Semiconductor detectors
Radiotherapy
Particle therapy

ABSTRACT

Spectroscopy-based photon-counting detector systems, Medipix, have many applications in medicine. Medipix detectors benefit from providing energy information as well as high spatial resolution. In this article, a review of Medipix detector technology applied to medicine and imaging techniques are presented. The technology has been used to develop quality assurance (QA) measurement devices in radiation-based treatments. A gamma camera system for radiotherapy has been developed to measure dose delivered to prostate treatments in real-time. The advantage of a high-resolution detector has been utilized in proton and heavy ion therapy for dose QA, measuring the charge particle spectra, and beam geometry for mini-beams. Applications in medical imaging using helium ion beams have been investigated to replace CT for ion beam radiotherapy. This technique provides many advantages over conventional CT such as high-resolution imaging and spectroscopy-based information for planning in helium ion treatments. The Medipix technology has shown it can be broadly applied in radiation and particle therapy applications for accurate QA as well as proving high-resolution imaging in medicine.

1. Introduction

This article explores the application of a high-resolution hybrid pixelated detector system, Medipix and Timepix in the field of medicine and imaging. Sections 2 and 3, discuss the use of Medipix in Brachytherapy for radiation dose quality-assurance (QA). Section 4 investigates using Medipix detectors in proton and heavy ion therapy for dose measurements, assessing charged particle spectra, and for beam geometry and intensity QA in mini-beams. Section 5 examines applications of medical imaging using helium ion beams and Timepix-based detector system.

2. Medipix of seed reconstruction and seed tracking (LDR and HDR) brachytherapy

2.1. BrachyView

Brachytherapy is an important therapeutic modality in modern cancer treatments and is used to treat prostate cancer patients. High Dose Rate (HDR) Brachytherapy involves placing a highly radioactive source such as Ir-192 at different locations inside the prostate to deliver planned dose to the tumor to kill the cancer cells. Low Dose Rate (LDR) Brachytherapy includes implantation of multiple I-125 seeds within the prostate to deliver a planned dose to the tumor (Voulgaris et al., 2008; Petasecca et al., 2013).

To ensure that the quality of source positions is accurate and

* Corresponding author.
E-mail address: anatoly@uow.edu.au (A. Rosenfeld).

https://doi.org/10.1016/j.radmeas.2019.106211
Received 19 May 2019; Received in revised form 16 August 2019; Accepted 21 August 2019
Available online 9 November 2019

effective at treating cancer, it is extremely important to provide effective QA measures and verification of source positioning during treatment. Currently, image guidance systems such as Trans Rectal Ultrasound (TRUS), Cone Beam Computed Tomography (CBCT), and C-arm CT machines are employed in cancer centres to provide image guidance of source positioning during treatment (Applewhite et al., 2001). These systems are limited in either resolution, lack of real-time image guidance, or delivering additional imaging dose to the patient (Batič et al., 2010).

The development of a seed-tracking system to monitor the location of sources in both LDR and HDR Brachytherapy is of high importance for better treatment quality. A proposed new imaging modality using a Medipix single photon counting system has the potential to resolve the HDR and LDR source during therapy by verifying the source placement and maintain an accurate dose delivery to the target organ (Soukup et al., 2011). The device, named BrachyView was developed at the Centre for Medical Radiation Physics (CMRP), the University of Wollongong, has been built to solve the issues with seed implantation verification. Using TRUS in conjunction with BrachyView will provide anatomical information as well as seed positioning information without giving any additional radiation to the patient for seed imaging.

Two BrachyView prototypes have been developed, HDR BrachyView and LDR BrachyView; each system consists of a detector housed in a tungsten cylindrical probe with truncated knife-edge multi-pinhole collimators, for verification and quality assurance of seed positioning during therapy and in treatment planning using an I-125 seed for LDR and Ir-192 source for HDR brachytherapy. The collimator designs for both probes were built from Monte Carlo studies to optimise the spatial resolution and sensitivity of the gamma camera system. The device is designed to be inserted into the rectum to image the seeds during treatment. The probe can reconstruct the position of a source in 3D using projections of the source through multiple pinhole collimators and a triangulation method. The centre of mass (CoM) of each projection is calculated based on the projection of the Brachytherapy source in each pixel of Medipix detector and then back-projected through the corresponding pinhole to determine the source location (Fig. 1).

2.2. High Dose Rate (HDR) brachytherapy

An edgeless quad Timepix detector assembly is embedded within the 4 mm thick tungsten collimator drilled with seven double cone pinholes (Fig. 2). Approximately 20% of the gamma photons from an Ir-192 source incident on a 4 mm thick tungsten slab will penetrate the collimator and reach the Medipix detector surface (Safavi-Naeini et al., 2015; Alnaghy et al., 2016).

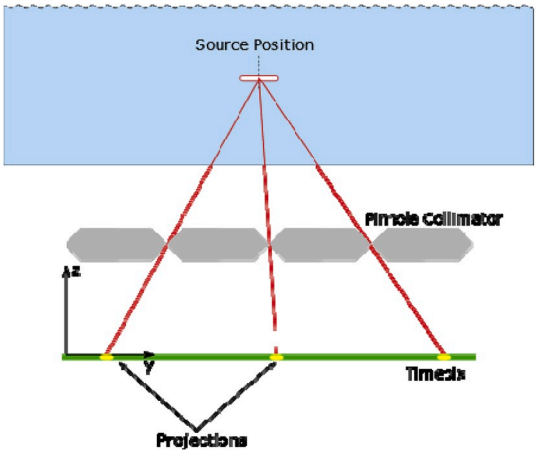

Fig. 1. Back projection method of BrachyView system. Seed/source projections through collimator on Timepix detectors are used to back projected line vectors and reconstruct the location of seed/source.

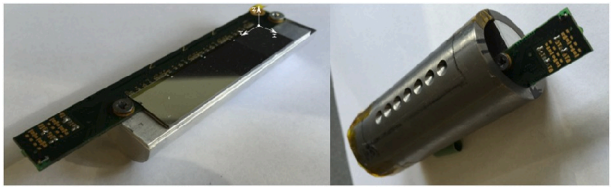

Fig. 2. Photo of HDR BrachyView probe prototype embedded with quad edgeless Medipix detector arrays.

Preliminary experiments have been performed using a custom tissue-equivalent PMMA block with a cylindrical slot to hold the HDR BrachyView probe. A custom solid water block was used to allow the catheter to be housed into a 2 mm diameter channel that runs halfway through the phantom block along the y-axis. The HDR treatment unit was connected to the catheter. Fig. 3 shows the experimental setup and treatment delivery used during the experiment. The dwell time was set to 20 s, with the BrachyView software set to acquire every 0.5 s in the frame by frame mode. A dummy seed was placed inside the catheter, and a CT scan was performing to validate the true position of the source during the delivery.

The planned source position validated by the CT scan shows the software was able to reconstruct the Ir-192 positions in the phantom (Fig. 4). The discrepancy between the reconstructed values and the planned positions were shown to be small, with 99% of the reconstructed values in the x, y and z-axis all within submillimeter to the planned source positions.

Future studies will evaluate the HDR BrachyView system using a full clinical treatment plan and a tissue-equivalent prostate gel phantom. TRUS imaging will be used to image the prostate and allow co-registration between the BrachyView and TRUS probes providing a fused Image of the prostate volume and reconstructed source positions.

2.3. Low Dose Rate (LDR) brachytherapy

The LDR BrachyView probe consists of three Timepix detectors housed in a 1 mm thick tungsten with single cone pinhole collimators (Fig. 5). The three Timepix detectors are placed directly beneath each of the pinholes. Since multiple seeds are implanted into the prostate, each seed is imaged at a minimum on two of the three detectors for the back-projection algorithm to reconstruct the locations of the implanted seeds.

Preclinical performance evaluation of the LDR BrachyView probe has been completed (Alnaghy et al., 2017). In this study, the prototype probe was placed in a clinical prostate gel phantom. The gel phantom was implanted with 30 I-125 seeds, guided using a TRUS system. The LDR BrachyView probe was used to image the 30 implanted seeds, the accuracy of the newly developed post-processing reconstruction algorithm using the BrachyView probe was evaluated. A CT scan of the gel phantom with the implanted seeds was performed and used as the reference data to identify the expected location of the seed positions (ground truth). The reconstructed positions of the seeds were co-registered with the TRUS coordinate system and rendered in a 3D volume using a custom-developed visualization software (Fig. 6).

The reconstructed seed positions measured by the LDR BrachyView probe demonstrate agreement with seed positions estimated by using a CT scan with a maximum discrepancy of 1.78 mm. It was observed that 75% of seed positions were reconstructed within 1 mm of their nominal location. Future improvements to the system involve implementing a real-time reconstruction algorithm embedded into the visualization software, providing seed positioning information in real-time and aiming to assist for intraoperative dynamic treatment planning in LDR brachytherapy.

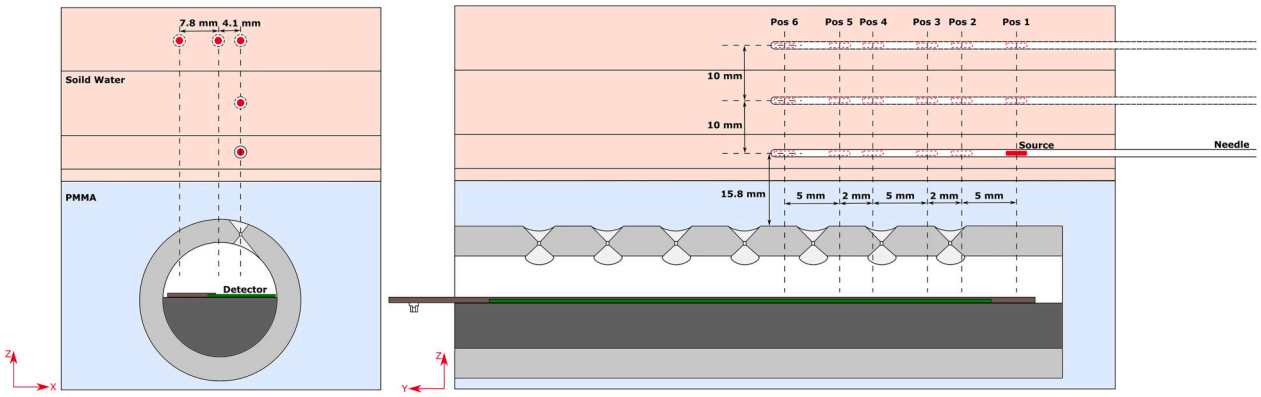

Fig. 3. Experimental setup of HDR BrachyView probe testing using solid water phantom to reconstruct source locations at various 3D locations.

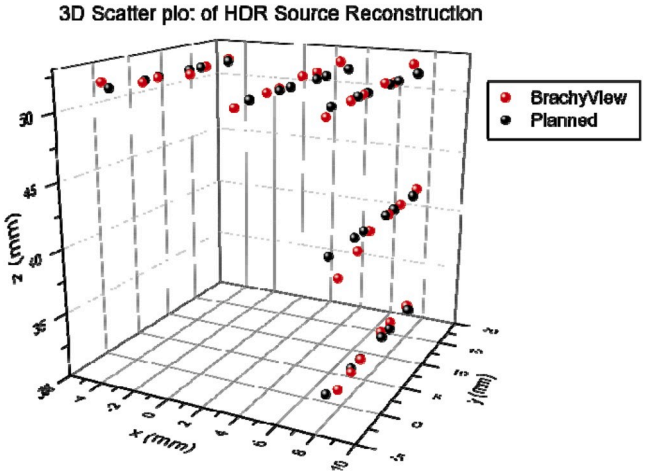

Fig. 4. Scatter plot of reconstructed 3D source positions from the HDR BrachyView probe, compared with ground truth seed locations based on CT scan of solid water phantom and TPS.

3. Medipix for eye plaque dosimetry

Melanoma and squamous cell carcinoma are the most common eye cancers in adults (Shields and Shields, 2009). Brachytherapy using radioactive eye plaques is the preferred method of treatment for patients with ocular malignancies. Eye Brachytherapy involves stitching a radioactive plaque behind the tumor on the eye, achieving local tumor control for eye melanoma. An important aspect of eye Brachytherapy is dosimetric QA is validating the activity and dose delivery of the eye plaques with the treatment planning system (TPS). The EyeCheck system developed at the CMRP utilises a single Timepix detector to identify the activity of each seed loaded into the plaque to determine the 3D dose distribution using the Amirian Association of Practice Management task group 43 (TG-43) protocol (Weaver et al., 2014). A prototype system has been developed to utilise spectroscopic dosimetry to generate a 3D dose map for QA checks (Fig. 7).

4. Medipix in proton and heavy ion therapy

4.1. Medipix2 for the characterization of a proton beamline

The capabilities of Medipix2 to characterize a proton beamline were studied working at the CATANA (Centro di AdroTerapia e Applicazioni Nucleari Avanzate, Center for Hadron Therapy and Advanced Nuclear Applications) beamline locate at the LNS-INFN laboratory in Catania-Italy (Cirrone et al., 2004). Here, since 2002, patients with ocular pathologies, like uveal melanoma, are treated using the 62 MeV proton beamline. The dose delivered to the patient and the proton beam quality is performed with a beam monitoring system: ion chambers for the dosimetric control, scanning diodes for the beam profile determination and GAF-chromic films for the physical characterization of the beam and the imaging of the irradiation field are used. A 2D single-photon counting detector as Medipix2 may reduce the long data acquisition time necessary to perform the beam quality measurements, and with this aim, a feasibility study was performed in 2008. Two test beams were performed to investigate the response of the system based on a pixilated silicon detector (300 μm thick) bump-bonded to the Medipix2 readout chip (MPX2MXR version). The active area was 2 cm^2 (256 × 256 square pixels), and a collimator placed at the end of the proton beamline was always adopted for the measurements. The experimental set up is

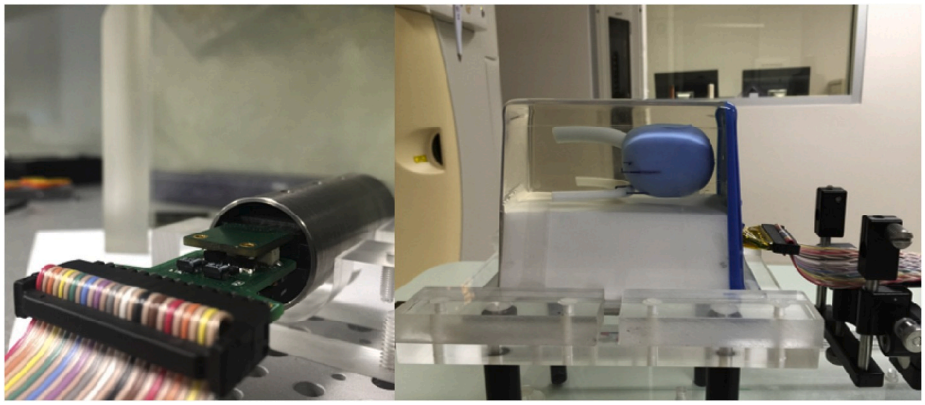

Fig. 5. Experimental setup of prototype LDR BrachyView probe placed inside prostate gel phantom to image 30 implanted I-125 seeds.

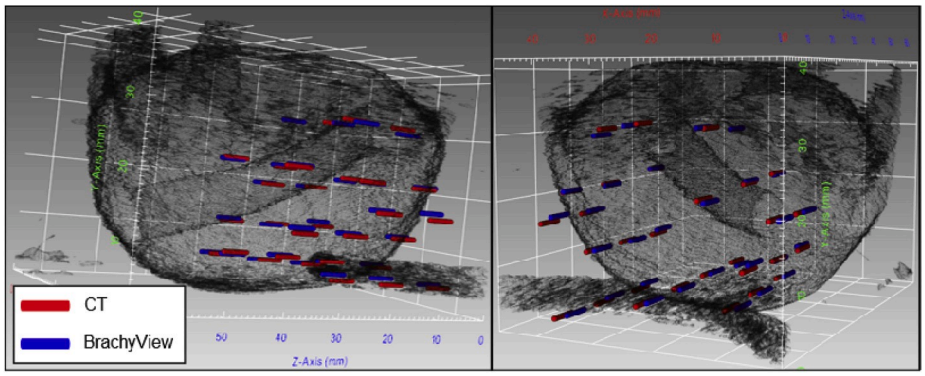

Fig. 6. 3D volume of prostate gel phantom from TRUS probe fused with reconducted seed positions (blue) from LDR BrachyView probe. Ground truth position (red) of the I-125 seeds was determined from CT image dataset. (For interpretation of the references to color in this figure legend, the reader is referred to the Web version of this article.)

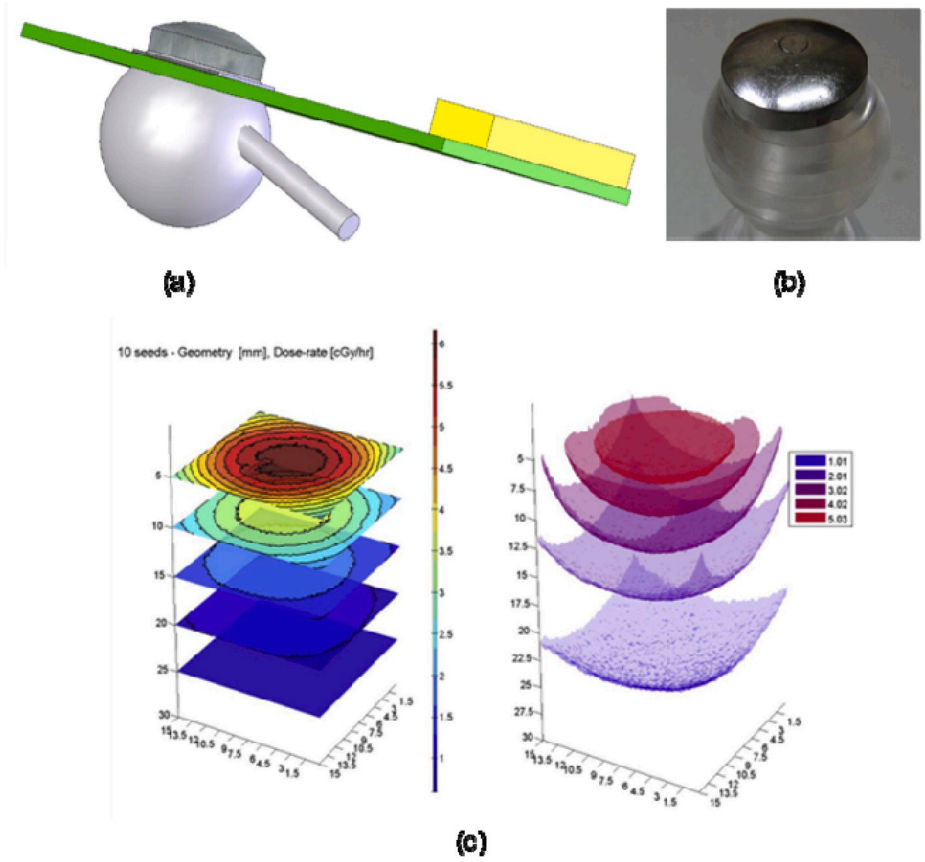

Fig. 7. a) Medipix2 board and eye phantom assembled; b) Multi-layer PMMA eye phantom; c) 3D Isodose surfaces in terms of counts and dose-rate for plaque loaded with 10 I-125 seeds.

reported in Fig. 8.

Preliminarily the detection system was calibrated and equalized: using radioactive sources, a uniform response from all pixels, when irradiated with a flat field, was obtained. The proton beam energy was set at 62 MeV (full energy), and the Medipix2 threshold was fixed at 113 keV (four standard deviations below the maximum energy released in silicon by 62 MeV protons). The Medipix detector response was studied as a function of delivered dose and exposure time. The linearity of the system concerning the delivered dose was checked using different dose rates. The response was linear up to 40 Gy/min where saturation effects start. It is worth noticing that the usual clinical dose rate at CATANA is 15 Gy/min. The linearity of the Medipix detector as a function of the exposure time was verified: for this measurement, a dose rate of 1.2 Gy/min was adopted and the maximum exposure time was set to 7 s. To verify the reproducibility of these measurements, each acquisition was repeated four times. For more details, see (Bisogni et al., 2008). The imaging capabilities of the systems were studied measuring some geometrical characteristics of the beam, as the lateral penumbra and the beam flatness. Due to the limited detection area, a collimator with a 5-mm-diameter hole was set at the end of the beam output (Fig. 8). After acquiring for few seconds the beam image, the profile along the *x* direction was extracted. The 2D beam image is reported in Fig. 9 left. The experimental points of the beam profile are reported as black squares in Fig. 9 right. To determine the rise and the fall of

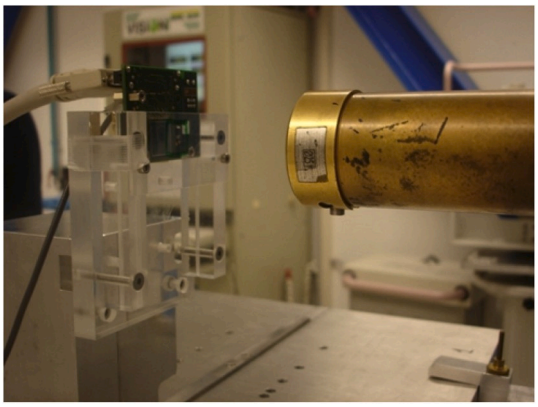

Fig. 8. The adopted experimental set up: on the left the Medipix2 system and on the right the beam output and the final brass collimator.

penumbra values, the data have been fitted with a double Boltzman function: the fit functions are reported as a continuous red line in Fig. 9 right. The rise lateral penumbra was 0.79 mm, while the fall one was 0.81 mm. The measurement error was 55 μm due to detector pitch. For comparison, the same quantities were calculated using a gafchromic film. The rise and the fall lateral penumbra resulted in 0.73 mm for both. In this case, the measurement error is 200 μm, due to digitalization pitch. The two sets of measurement gave the same results within the errors. Using the same beam profile of the preceding measurement, the beam flatness was evaluated, and a value of 3% for both systems was determined. For more details, see (Bisogni et al., 2009).

As a conclusion, measurements performed with a detection system based on Medipix2 readout chip for the characterization of the CATANA beam were performed and compared concerning those obtained using routine systems in the same experimental conditions. Being the results in very good agreement, we can conclude that the proposed detection system can work as a single proton counter. More extensive measurements are necessary to confirm that the system can be used as a routine detection system.

4.2. Monitoring of radiotherapeutic carbon ion beams using a Timepix detector

The physical and radiobiological properties of therapeutic ion beams allow for an increased dose conformation to the tumor in comparison to standard radiotherapy with photon beams (Schardt et al., 2010a). This enables an increased sparing of the surrounding healthy organs. However, the superior dose distributions, theoretically achievable with ions, are often compromised by uncertainties on the actual stopping power of patient's tissue. They include geometrical uncertainties (due to patient positioning, weight gain or loss, swelling of tissue, and possible movement) and uncertainties on tissue's composition (due to its measurement using photon attenuation in CT images) (Baumann et al., 2016). The uncertainties from these sources translate into the size of safety margins around the target, which are designed to assure that the tumor receives the planned dose. However, the larger the margins, the larger is the irradiated volume of the surrounding healthy tissue. This might lead to an increased rate and severity of side effects. As a result, the maximal dose, which can be realistically applied to the tumor is limited. Therefore, methods providing information on the delivered dose distribution in the patient are highly desired.

4.2.1. Non-invasive in-vivo beam monitoring using secondary ions

An accurate method for an in-vivo visualization of the radiation field within the patient's anatomy during treatment represents an ultimate verification of the whole therapeutic chain. The first generation of such monitoring techniques was based on the determination of the beam-induced activation of the patient's tissues, as measured by positron emission tomography (PET) cameras (Enghardt et al., 2004; Shakirin et al., 2011). Due to the limited spatial resolution, much lower signal than in PET diagnostics, its washout by blood flow, no real-time signal and in some cases discomfort for the patient due to long measurement times, alternative approaches are of major interest for the community. However, second-generation in-beam-PET scanner have demonstrated on flight reconstruction of the activity distribution acquired during the irradiation (Ferrero et al., 2018).

Prompt secondary radiation, including photons and secondary ions is another product of the nuclear interactions of the beam in the patient. It is emitted instantaneously during irradiation. Thus, it is insensitive to smearing due to physiological washout processes. Prompt photons exhibit energies of several MeV. Therefore, the measurement of their direction represents a large challenge. Secondary ions (Dauvergne et al., 2009; Amaldi et al., 2010) are straight forward to detect. However, efficient, clinically applicable detector prototypes are presently lacking.

4.2.2. Experiments and setups

These studies aimed to determine the pattern of the secondary ion emission from the object irradiated with therapeutic carbon ion beams and to identify changes in the secondary ion emission with intentional variations of the object's geometry or variations of the treatment beam. The experiments were performed at the Heidelberg Ion-Beam Therapy Facility (HIT) in Germany. Narrow, pencil-like carbon ion beams typically for head treatments were directed onto patient models with different complexity, ranging from a homogeneous plastic cylinder

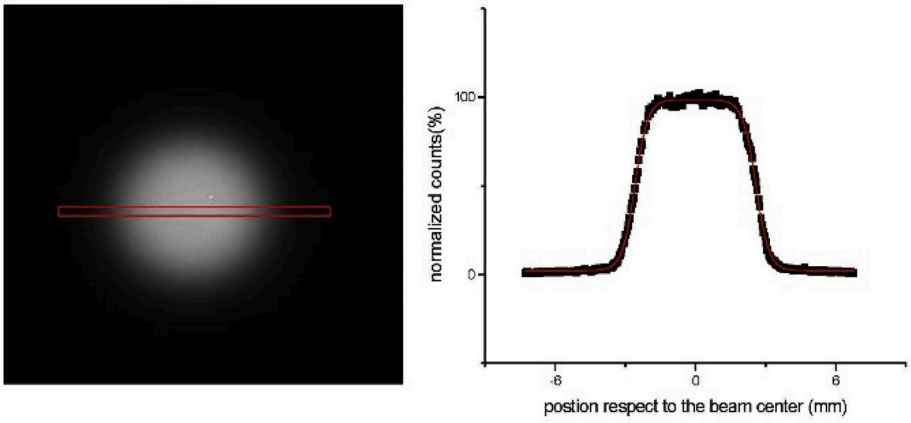

Fig. 9. The 2D beam image (left) and the extracted profile with the double Boltzmann function in red (right). The red rectangular on the beam image represents the zone where the profile was calculated. (For interpretation of the references to color in this figure legend, the reader is referred to the Web version of this article.)

(Gwosch1 et al., 2013; Reinhart et al., 2017), plastic phantoms containing 1–3 cm large inhomogeneities (Reinhart et al., 2017; Gaa et al., 2017) and an anatomic model of a human head (Alderson phantom) (Alderson et al., 1962) containing real bones and tissue-equivalent materials.

The suitability of a flexible and handy mini-tracker composed of a pair of Timepix detectors (Ballabriga et al., 2007), later also Timepix3 (Poikela et al., 2014), detectors for determination of the spatial distribution of paths of secondary ions, which are emitted around the irradiated objects during the beam delivery, was investigated as shown in Fig. 10.

4.2.3. Results and discussion

The Timepix-based detector was found to be suitable to efficiently track the secondary ions emerging from the patient-sized objects irradiated by therapeutic carbon ion beams. In the situation studied, a correlation of the emission pattern (Fig. 10 right) with the intentional changes of the beam width, position, and energy were shown experimentally for single pencil carbon ion beams (Gwosch1 et al., 2013). Moreover, the method was shown to be capable of visualizing air cavities of the size of down to 1 cm in the irradiated plastic patient model (Reinhart et al., 2017; Gaa et al., 2017). The sensitivity to inhomogeneities was demonstrated, even when the inhomogeneity was positioned at large depths, like directly in front of and even behind the Bragg peak (Gaa et al., 2017).

Finally, from track measurements at several angles concerning the beam axis, a 3D image of the beam in the phantom was reconstructed using a maximum likelihood expectation-maximization algorithm (Reinhart et al., 2017). An example is shown in Fig. 11 (left), clearly visualizing the circular air-filled inhomogeneity. Moreover, Fig. 11 (right) shows quantitatively that the filling material of the cavity could be distinguished, even for small density differences like in the case of plastic and adipose tissue surrogate.

The largest drawback of Timepix for this application was the dead time, which amounted to more than 90% of the irradiation time. The very recent results obtained with a Timepix3 tracker highlight the value of its deadtime-free operation. Fig. 12 depicts an example of a measurement of the lateral position of the scanned carbon ion pencil beam. The beam delivery was mimicking a therapeutic treatment with typical tumor size, position, and dose to a human-like phantom (Alderson head phantom). In Fig. 12, the pencil beam scanning can be clearly followed. Moreover, a close correlation to the actual pencil beam's position, as determined by the monitoring chambers installed in the beamline, is visible.

The capability of single ion tracking, which is accessible also to applied physics fields like medical physics due to Timepix and Timepix3, enabled us to perform several subsequent research steps in the novel field of carbon ion treatment monitoring using emitted secondary ions. The improved tiltability and even higher temporal resolution of Timepix4 (Campbell et al., 2016) go in-line with the needs of this field while bringing this new method to the patient.

4.3. Charged-particle tracking and spectrometric characterization of mixed radiation fields

4.3.1. Quantum-imaging detection, online track visualization

The photon-counting sensitivity, dark-current free operation, high granularity, and per-pixel energy sensitivity enable operation of the Timepix detector as an active nuclear emulsion (Poikela et al., 2014; Campbell et al., 2016). The Timepix detector provides quantum-imaging detection and track visualization of single particles valuable for high-resolution and wide-range spectral- and directional-sensitive characterization of mixed radiation fields such as those encountered in space (Vykydal et al., 2006; Granja and Pospisil, 2014) and in ion beam radiotherapy environments (Granja et al., 2016; Stoffle et al., 2015; Jakubek et al., 2010). Use of compact instrumentation enables to perform flexible and online measurements. Data products include particle fluxes, dose rates, time- and spatial-dose distributions (Martisikova et al., 2011) and LET spectra (Granja et al., 2018a). Discrimination between primary beam particles from secondary and background components (Stoffle et al., 2015; Gehrke et al., 2017) enables to map the yield and extent of beam fragmentation (Opalka et al., 2013; Jakubek et al., 2011a; Gallas et al., 2017a).

4.3.2. Compact radiation cameras, sensor stack architectures

The sensitivity of the Timepix detector is 100% for charged particles, both light and heavy charged particles including minimum-ionizing-particles (MIPs) (Granja et al., 2018a; Hartmann et al., 2017). X-rays and gamma rays are detected above a few keV and with decreasing efficiency up to tens or few hundreds of keV depending on the sensor material and thickness (below). For wider sensitivity to X-rays and gamma rays, as well as enhanced tracking resolving power for charged particles, the Timepix detectors can be equipped with different semiconductor sensor material (Si, CdTe, GaAs) and thickness (100–2000 μm). Ease of detector operation and convenient deployment are made possible by compact readout interfaces which vary in size and frame readout speed (from few frames per second (fps) up to few hundred fps) such as FITPix (Hartmann et al., 2012), USB-Lite (Granja et al., 2013), MiniPIX (Jakubek et al., 2010; Kraus et al., 2012) shown in Fig. 13a, and ModuPIX (Turecek et al., 2011a). Besides the single-chip miniaturized radiation cameras (USB-Lite, MiniPIX-TPX), the Timepix ASIC-chip assemblies can be arranged in compact stack array architectures such as 2 × layer TPX stack (Miniaturized readout inte, 2016; High frame rate parallel, 2015) and as a gapless 4 × layer TPX WidePIX-3D micro-tracker illustrated in Fig. 13c. The compact radiation cameras are controlled by integrated software tool Pixelman (Soukup et al., 2011) and PIXET (Jakubek et al., 2011b) which run on multi-platforms/PCs and mini-computers running Windows/Linux/MacOS operating systems. The software tools provide data

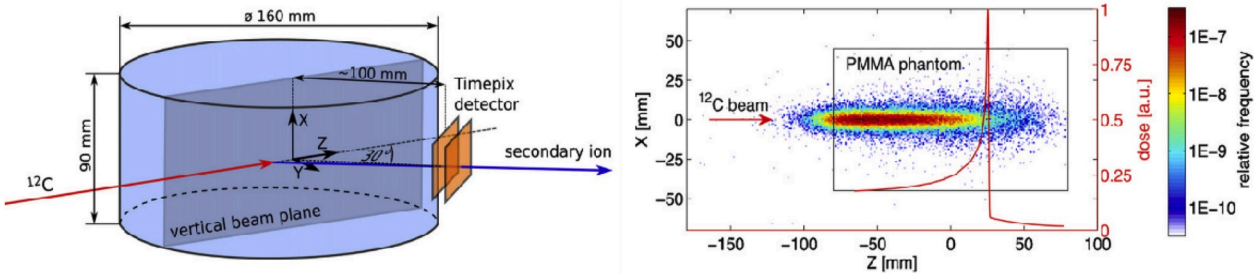

Fig. 10. Left: Illustration of the experimental set-up. A cylindrical head-sized plastic phantom is irradiated with a carbon ion pencil beam typical for therapy. Emitted secondary ions are detected with a double-layered Timepix mini-tracker placed at 30° concerning the beam axis. Right: The color scale represents the distribution of the back-projected measured tracks. The cylindrical phantom from the left image is illustrated by the black rectangle (side view). The red curve shows the corresponding depth dose distribution. Both images reprinted from (Gwosch1 et al., 2013). (For interpretation of the references to color in this figure legend, the reader is referred to the Web version of this article.)

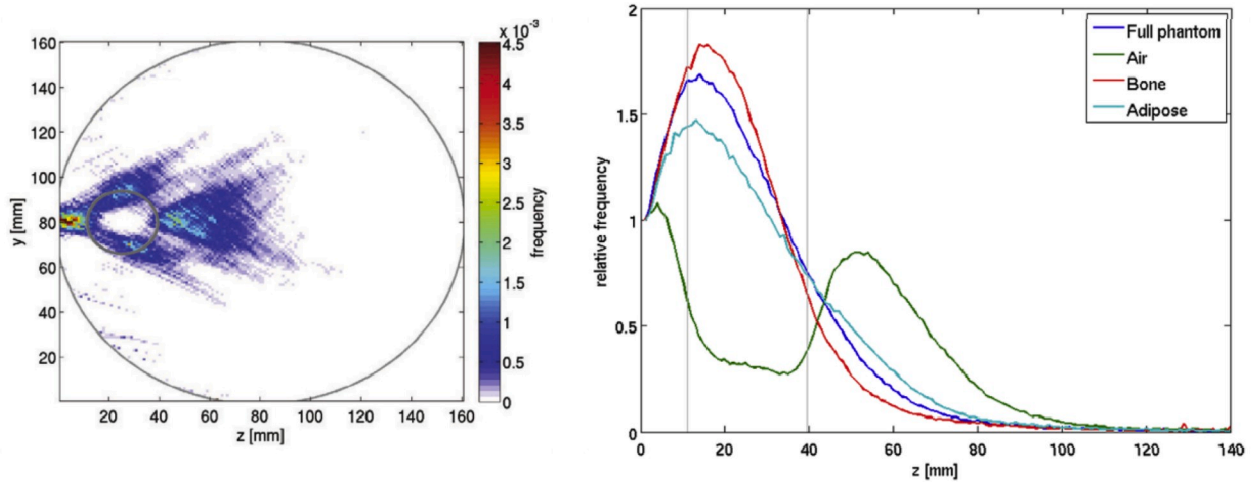

Fig. 11. Left: Image of the carbon ion pencil beam with an energy of 226 MeV/u incoming from left to right in a cylindrical plastic phantom visualized by the large circle (top view). The small gray circle with a diameter of 2.85 cm depicts the localization of a cylinder-shaped cavity filled by air. Right: profiles through reconstructed beam images for three different fillings of the cylindrical cavity, and a homogeneous phantom cylinder (side view). All the cases can be differentiated. Both images reprinted from (Reinhart et al., 2017).

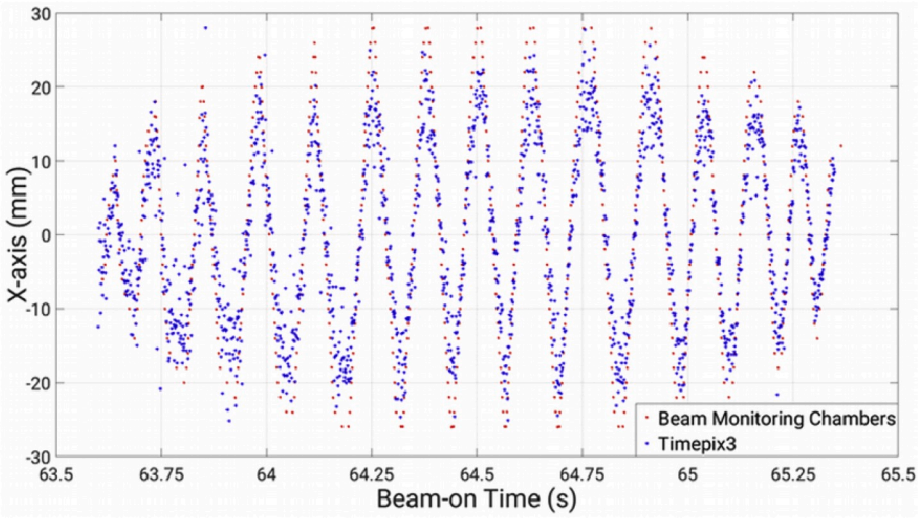

Fig. 12. Pencil beam scanning: comparison of the lateral pencil beam position as measured by the beam application system (reference) and measurements by a Timepix3 tracker using the emitted secondary ions. The Timepix detector was positioned next to a human-like head model, at 30° concerning the beam axis. The pencil beam position was determined as the center of mass of the measured secondary ion tracks. A quantitative comparison is feasible only within a few mm around x = 0 mm, due to the given geometric acceptance of the minitracker with a sensitive area of $14 \times 14\,mm^2$ only — image by Renato Felix Bautista (DKFZ).

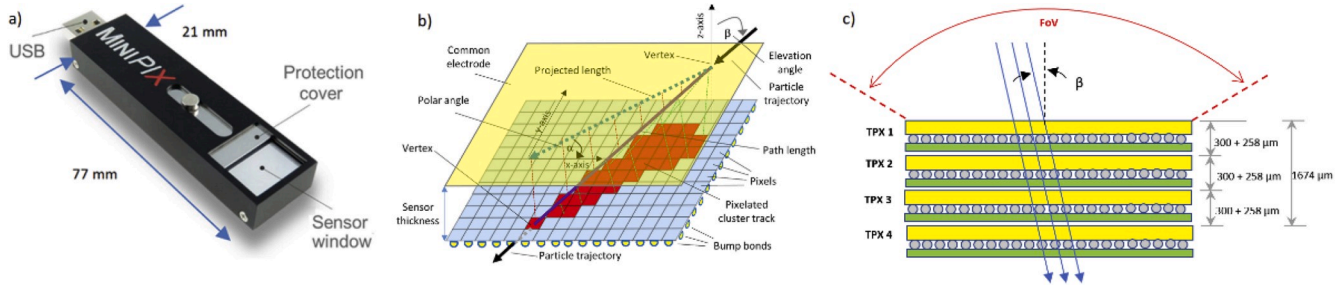

Fig. 13. (a) The miniaturized readout interface MiniPIX (c) has dimensions 77 mm × 21 mm × 10 mm connects directly to PC or laptop via USB port. (b) Illustration of particle tracking for energetic charged particles. Micro-scale pattern recognition analysis of the registered signal (cluster of pixels –shown in red) enables deriving the path length in 3D (purple line) and direction (see polar and elevation angles α and β). (c) Illustration of miniaturized wide field-of-view (FoV) particle microtracker consisting of 4 × Timepix layers with minimal spacing gaps providing a compact particle telescope WidePIX-3D. (For interpretation of the references to color in this figure legend, the reader is referred to the Web version of this article.)

readout and online response.

4.3.3. Wide-range detection and characterization of mixed-radiation fields

Studies have been performed at the ion synchrotrons at HIT-Heidelberg and HIMAC-Chiba. Measurements in air and with tissue-equivalent phantoms of PMMA and water tank using protons and light ions with energies above few tens of MeV/u (Stoffle et al., 2015; Turecek et al., 2011b; Turecek and Jakubek, 2015). The detection and track visualization of pixelated clusters registered by various charged particles at selected energy and direction are shown in Fig. 14. Timepix registers the deposited energy along the trajectory across the sensor. Together with the track path (Fig. 13b), registered in 3D, the linear-energy-transfer LET is derived. The wide dynamic range of per-pixel electronics allows measuring high- and low-LET particles. For high-Z particles, a distortion and saturation of the per-pixel energy registration arises (Arico et al., 2017; Martisikova et al., 2018; Granja et al., 2011), which can be partly corrected by tuning the sensor bias and the Timepix ASIC DAC settings (Jakubek et al., 2010; Arico et al., 2017). The Timepix detector can be further calibrated to better describe the saturation effects as performed with monoenergetic protons (Granja et al., 2011; Hartmann et al., 2014).

4.3.4. Resolving power, dynamic range, wide field-of-view

The resolving power of the Timepix detector is analyzed in terms of particle-type (species), spectral response (energy loss) and directional sensitivity (no collimators needed) (Jakubek et al., 2010, 2011a; Gallas et al., 2017a; George et al., 2018). The analysis is based on morphology and spectrometric analysis and tracking information of the pixelated clusters. The resolving power is based on pixel cluster morphology analysis together with the per-pixel energy and tracking information (Granja et al., 2018a; Hartmann et al., 2017) including resulting LET spectra. The resolution is enhanced by correlated analysis of cluster analysis parameters (Kroupa et al., 2014) of single parameters (Jakubek et al., 2010; Gallas et al., 2017a) such as cluster size (number of pixels in the cluster) and cluster volume (sum of the per-pixel energies in the cluster) as shown in Fig. 15. The resolution is further improved by correlated analysis of elaborated parameters such as cluster height (largest per-pixel energy in the cluster) convoluted with the cluster length together with the LET (Jakubek et al., 2010; George et al., 2018) shown in Fig. 16. Work performed spans a wide range of heavy charged particles in a wide range of energies including energetic heavy charged particles and MIPS. For certain parameters, event-type regions may in part overlap, especially at extreme values. This is the case for energetic protons in the MIP regime. Therefore, the broad scope of discrimination is achieved together with the tracking and morphology information. The resulting physics-based classification of broad-types events is derived (Jakubek et al., 2010) in terms of radiation main components/species (X-rays, light and charged particles of low- and high-energy), spectral/stopping power (dE/dx, LET spectra over several bins in semi-log range) and direction in wide field-of-view (essentially 2π). The dynamic detection range includes energetic heavy charged particles and minimum ionizing particles (George et al., 2018).

Further sub-classification of heavy charged particles into ion groups (such as light, medium-mass and heavy ions) is ongoing by more extensive and elaborate analysis of the pixelated tracks. This research merges with challenging tasks towards ion and reaction product identification (Jakubek et al., 2011a) as well as efforts to derive information on the charge and velocity of highly energetic heavy ions by detection and analysis of accompanying delta electrons registered in Timepix (Pinsky et al., 2011). Advanced techniques aim at determining and evaluate Timepix's sensitivity to the ion total kinetic energy, which is being explored in space radiation detection data (Granja et al., 2018b; Pinsky et al., 2011; Stoffle et al., 2012). Another development direction makes use of stacked arrays of two and more Timepix detectors in telescope architecture (Miniaturized readout inte, 2016) for enhanced discrimination of neutrons (Gehrke et al., 2017) and mixed radiation fields (Gehrke et al., 2017; Stoffle and Pinsky, 2018) as well as high angular resolution directional detection of energetic charged particles (High frame rate parallel, 2015). A single layer Timepix detector has also directional response (Granja et al., 2018c) with limited angular resolution.

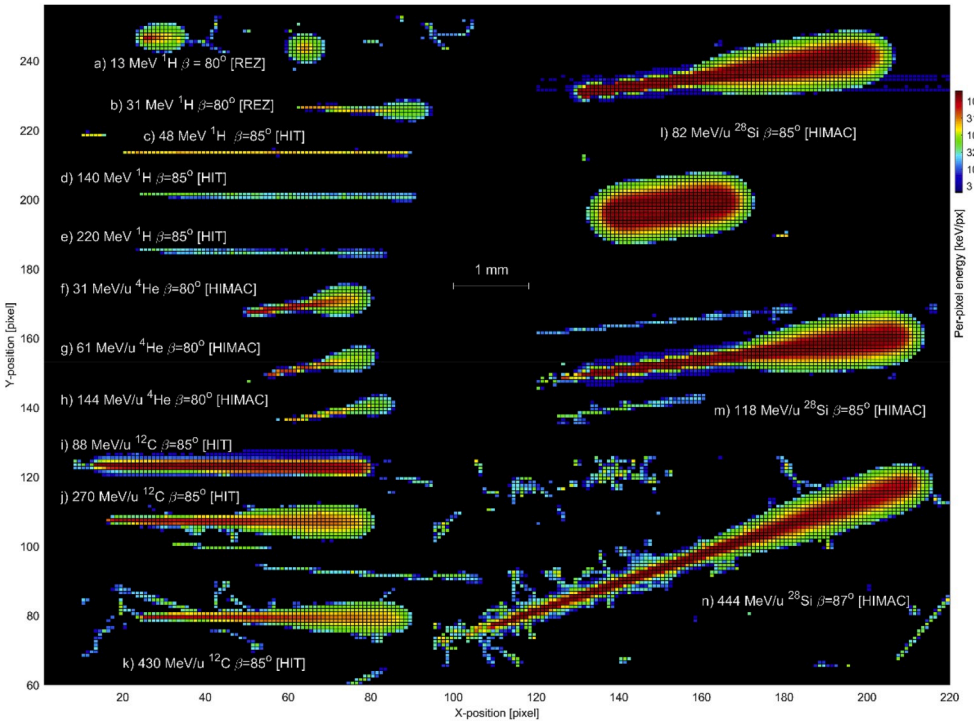

Fig. 14. Detection and track visualization of protons and low- and medium-Z ions at selected energies and incident elevation angle β – see labels, incident from right to left: protons of 13 and 31 MeV (cyclotron at NPI-CAS, Rez), 48, 140 and 220 MeV (synchrotron at HIT, Heidelberg), 4He of 31, 61 and 144 MeV/u (synchrotron at HIMAC, Chiba), 12C ions of 88, 270 and 430 MeV/u (synchrotron at HIT, Heidelberg), 28Si ions of 82, 118 and 444 MeV/u (synchrotron at HIMAC, Chiba). Additional events are displayed, such as background and correlated light ion secondary products (accompanying the 12C and 28Si particles). A portion (220 x 190 pixels = 1.28 cm2 or about 2/3 of the whole sensor area) of the pixel matrix are shown. Measured by a MiniPIX-Timepix camera equipped with a 300 μm silicon (shown in Fig. 1a). The sensor bias was 30 V except c) set at 100 V. The per-pixel energy response are shown in color log scale. Taken from (George et al., 2018). (For interpretation of the references to color in this figure legend, the reader is referred to the Web version of this article.)

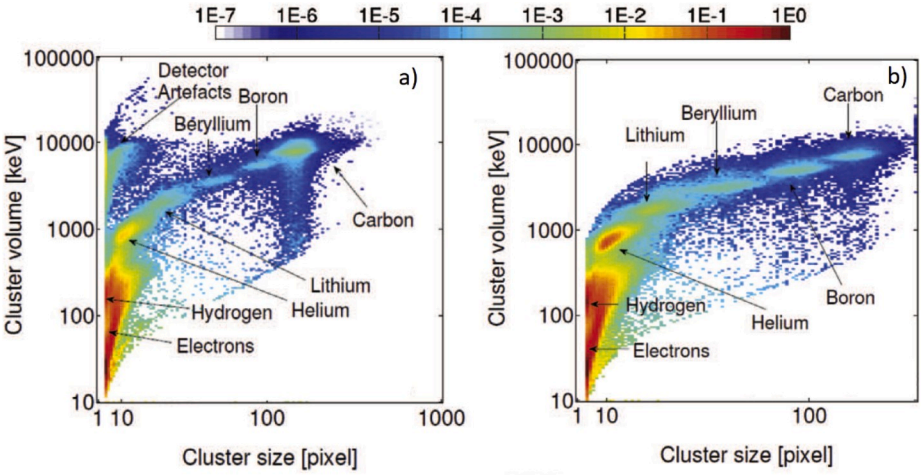

Fig. 15. Correlated analysis of cluster parameters size (number of pixels in a cluster) and volume (sum of per-pixel energies) for a 12C beam of energy (a) 271 MeV/u and (b) 400 MeV/u behind (a) 50 mm PMMA and (b) 158 mm water tank. Events per bin are shown in color in log scale. Measured by a single Timepix detector with 300 μm Si sensor at HIT-Heidelberg. Taken from (Jakubek et al., 2011a). (For interpretation of the references to color in this figure legend, the reader is referred to the Web version of this article.)

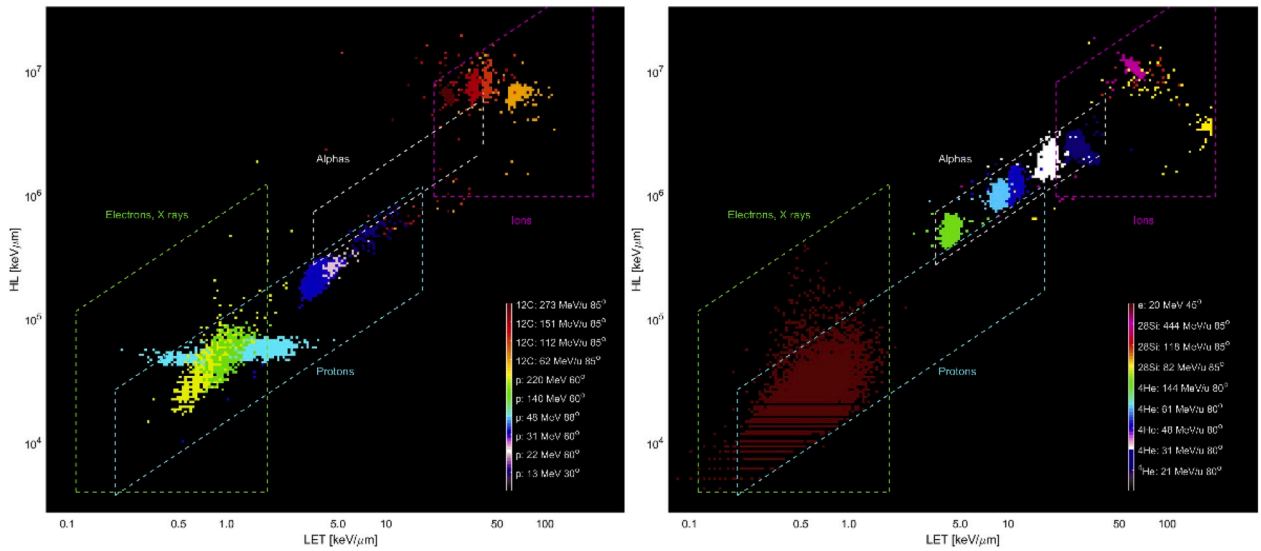

Fig. 16. Resolving power of Timepix to (a) protons and 12C ions and (b) alpha particles and 4He and 28Si ions at varying energies and incident angles. 2D-scatter/correlated plots (event histogram) of cluster analysis parameters (Height × Elevation Angle (HEA) vs Linear Energy Transfer (LET)). Measured by a single-chip MiniPIX-TPX camera (300 μm Si sensor) at HIT-Heidelberg and HIMAC-Chiba. Electron data from the microtron accelerator at the NPI-CAS Prague are included. Identified regions of particle types are given for the studied energies. Taken from (Granja et al., 2018b).

4.4. Timepix for the reconstruction of proton spectra in laser-driven proton acceleration

With the continued advances in the development of high-power laser systems, laser-driven proton acceleration might become a viable technique to produce protons with energies suitable for biomedical applications. Laser-accelerated proton bunches exhibit some remarkable features as compared to conventionally accelerated beams, such as a broad energy distribution ($\Delta E/E \sim 100\%$), a source size in the order of some micrometers and beam divergence angles typically ranging from a few up to a few tens of degrees. Bunch charges in the order of a nanocoulomb, combined with the initial bunch duration in the order of a picosecond, result in enormous particle fluxes. Hence accurate and efficient online characterization of such laser-accelerated proton bunches is still a challenging task, and various approaches have been proposed recently (Daido et al., 2012).

A first attempt to use Timepix detectors for the diagnostic of laser-accelerated particles was performed by (Reinhardt, 2012), however concluding that this detector is not suited in conventional face-on irradiation due to its limited dynamic range and the high proton fluxes. Nevertheless, a convenient alternative approach for spectrometry of polyenergetic proton bunches is based on edge-on irradiation of the Timepix detector. Here, the sensor chip surface is positioned parallel to the proton beam direction. In such configuration, the energy deposition of all protons along their paths inside the sensor chip is measured. The Timepix detector can, therefore, be used as a silicon-based range telescope that additionally provides position information along one transversal dimension (Würl, 2018). A sketch illustrating the principle of Timepix edge-on spectrometry is shown in Fig. 17. To ensure centric and perpendicular incidence of the protons concerning the front edge of the 500 μm thick silicon sensor chip, a 150 μm thin slit between two aluminum blocks was used as a collimator in a first prototype setup. To reduce stray radiation and electromagnetic noise, the Timepix detector was placed inside a dedicated aluminum housing. The Timepix detector was operated in time-over-threshold mode and was energy-calibrated according to the procedure described in (Jakubek, 2011).

For a sufficiently high proton flux, the individual proton tracks are overlapping, and the measured detector signal hence becomes the superposition of the energy deposition by many individual protons along with their entire penetration depth inside the sensor chip. Thus, for

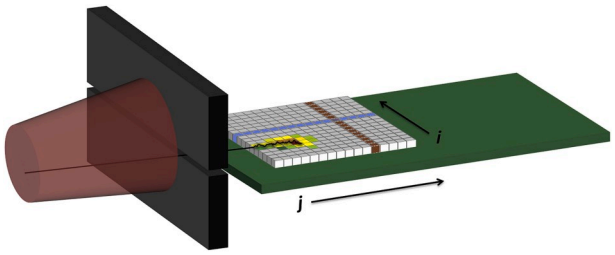

Fig. 17. Sketch showing Timepix edge-on spectrometry. The proton bunch coming from the left (red cone) is hitting the collimator (black blocks). The sensor chip of the Timepix detector is shown in gray. Only a small number of protons (indicated by the black line) pass through the slit and impinge on the sensor chip's front edge. The individual protons penetrate the sensor chip parallel to its face and are continuously slowed down, resulting in a signal inside the traversed and neighboring pixels proportional to the energy deposition (indicated by colors in pixels ranging from green to red). One of the pixel columns is colored blue, and one-pixel row is marked in brown to explain the nomenclature used here. Figure is taken from (Würl, 2018). (For interpretation of the references to color in this figure legend, the reader is referred to the Web version of this article.)

every pixel column i (perpendicular to the irradiated edge), the Timepix detector signal S_{ij} in the pixel row j (parallel to the edge) can be written as:

$$S_{ij} = \sum_k n_{ik} \cdot A_{jk} \tag{1}$$

where the matrix elements A_{jk} are given by the average energy deposition of one proton with kinetic energy k within one pixel of the row j and n_{ik} is the number of protons within a certain energy bin k. The equation system can be solved by means of linear least-squares optimization, provided that the matrix A is properly set up. To this aim, the sensor chip of the Timepix detector was irradiated at a Tandem van-de-Graaff accelerator with a proton beam of energies ranging between 17 and 20 MeV. The beam current was reduced to a minimum, such that individual proton tracks could be identified and extracted from the measured Timepix frames. Thus, for each proton energy, about 1000 individual tracks were extracted and averaged, resulting in one model track for every discrete experimental energy. For other kinetic energies, model tracks were obtained by interpolation and extrapolation. These tracks are then used to set up the matrix A, as shown in Fig. 18.

First experiments using this prototype Timepix edge-on spectrometer were performed using a 20 MeV proton beam from the Tandem accelerator and a small sample consisting of four partially overlapping layers of radiochromic film attached to the entrance slit of the spectrometer. This sample provides a laterally varying energy distribution at the location of the sensor chip. The measured detector signal is shown in Fig. 3 (top), and the corresponding reconstructed energy distribution is plotted in Fig. 3 (bottom). To reduce computation time, four adjacent pixel columns were combined to one.

However, typical proton fluxes from laser-driven proton sources can easily exceed the saturation limit of the Timepix detector. Moreover, particles that leave the sensor chip due to elastic Coulomb scattering or protons that experience nuclear interactions are not accounted for in this approach and can, therefore, bias the reconstructed energy spectrum. A possible solution to overcome these limitations relies on the detection of particles scattered within an absorber slab (e.g., PMMA) mounted on top of the sensor chip. This approach is based on a study performed by (Merchant et al., 2017). By adjusting the slit such that the incoming protons all penetrate the absorber and with appropriate slab thickness and absorber material, the number of protons reaching the sensor chip can be well controlled, and spectrometry of laser-driven proton bunches can be performed.

4.5. *Timepix for most likely path verification in proton computed tomography studies*

Proton computed tomography (pCT) is a promising imaging technique to substitute x-ray computed tomography for more accurate proton therapy treatment planning, reducing the uncertainty in the proton range determination. Currently, Hounsfield values in x-ray computed tomography are converted to relative stopping power in proton treatment plans, leading to 3%–5% systematic errors in the proton range calculation (Schaffner and Pedroni, 1998). PCT provides a possible solution to this uncertainty providing a direct calculation of the proton relative stopping power from proton energy loss measurement, thus reducing the uncertainty to less than 1% (Schulte et al., 2004). In 2013–2015 a new pCT scanner was built by the pCT collaboration formed by Loma Linda University and University of California Santa Cruz. The scanner consists of a tracking system (silicon strip detector), measuring the coordinates of protons entering and exiting the scanned object, and a scintillating energy detector, measuring the protons residual energy (Johnson et al., 2016; Bashkirov et al., 2016).

Penfold et al. (2010) developed an image reconstruction algorithm based on algebraic reconstruction technique combined with a most likely path (MLP) formalism (Schulte et al., 2008), predicting the proton path of maximum likelihood, to improve the pCT spatial resolution in pCT image reconstruction. The MLP formalisms currently available in the literature (Schulte et al., 2008; Williams, 2004) assume that the traversed medium is homogeneous (typically water or water-equivalent material). But in heterogeneous medium (i.e., patients), protons have different behaviors when traversing materials of different densities, scattering more in a dense material than in the less dense material and multiple Coulomb scattering causes Bragg peak degradation (Sawakuchi et al., 2008) (see Fig. 19).

To investigate the effect of heterogeneities in the pCT image reconstruction algorithm, Timepix was used to compare the experimentally measured proton path with the MLP predicted one. Timepix was successfully integrated with the prototype pCT scanner, and Fig. 20 shows the experimental setup used for this study. A human chest configuration

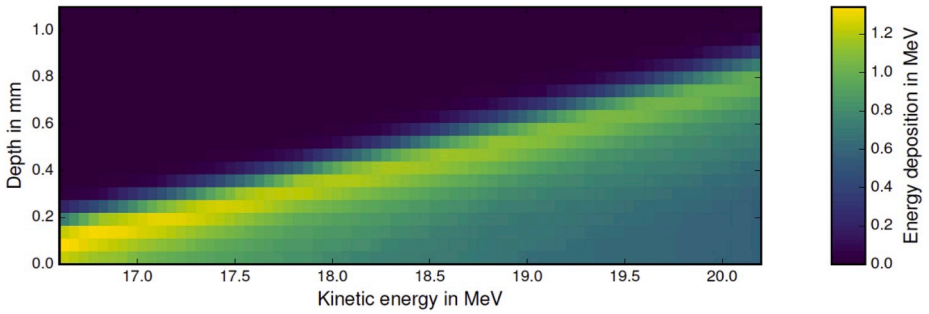

Fig. 18. Graphical representation of the matrix A for spectrum reconstruction. Every column corresponds to the laterally integrated average energy deposition in the sensor chip for one proton of a certain energy; figure is taken from (Würl, 2018).

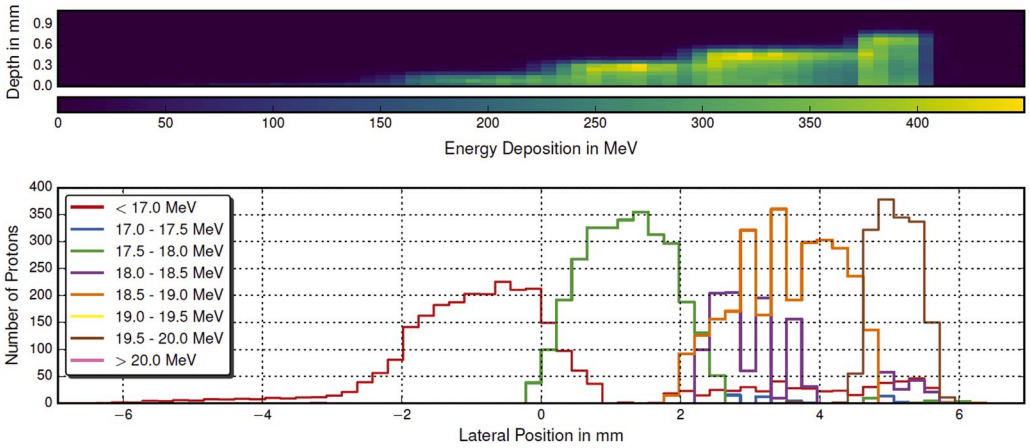

Fig. 19. Measured Timepix signal (top) and reconstructed lateral energy distribution (bottom) for a sample consisting of four partially overlapping layers of radiochromic film. In the Timepix frame, only the first 16 pixel rows are shown as the signal in the more distal rows is zero, the figure is taken from (Würl, 2018).

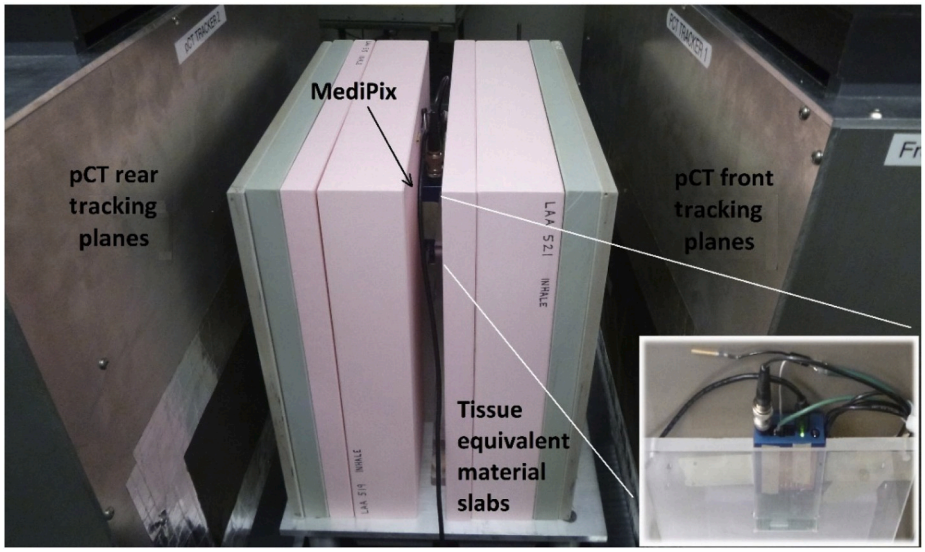

Fig. 20. Experimental setup for the Timepix -pCT study. The Timepix was held between the slabs of a custom made PMMA plate (insert) in the center of the chest slab phantom: 2 slabs of the lung (7 cm), one slab of soft tissue (2 cm) and one slab of cortical bone (1 cm) (Giacometti et al., 2017).

(here referred as "chest slab phantom") was created by symmetrically arranging tissue-equivalent slabs (CIRS, Norfolk, VA) of cortical bone, soft tissue, and lung on either side of the phantom center. Timepix was located at the center of the chest slab phantom, held by a custom made PMMA plate. Timepix measurements without slabs were conducted as well. Timepix consisted of a 150 μm silicon detector chip covering an area of 1.5×1.5 cm^2, operating in Time of Arrival and controlled via the Pixelman software package (Turecek et al., 2011c). The pCT scanner firmware was modified to use Timepix and pCT time stamps to match Timepix and pCT proton signal.

The proton MLP was calculated using the coordinates of the hits at entrance and exit tracking planes, according to the formalism described by Schulte et al. (2008). The accuracy of the prediction Δ(MLP) was calculated, as the difference between measured and predicted MLP, for horizontal and vertical coordinates independently. Table 1 shows the mean and standard deviation (StdDev) of Δ(MLP) along *x* and *y* direction for Timepix alone and chest slab phantom configuration. The agreement between experimental and predicted measurements was always within one standard deviation, and the MLP algorithm was not significantly affected by heterogeneities. Other studies were conducted evaluating the protons MLP accuracy with inhomogeneous phantoms, but the novelty of the work here presented is the use of experimental data collected with a high spatial resolution pixelated detector (Wong et al., 2009). Timepix was proven to be a very simple and useful tool for this investigation on pCT.

Future pCT – Timepix studies include the study of other "clinical" configurations, the investigation of the MLP angular dependency and the integration of this work in the pCT software simulation platform presented in (Giacometti et al., 2017).

Table 1
Calculated Δ(MLP) ± standard deviation (StdDev) along x and y-axis.

Configuration	Δ(MLP)x ± StdDev [mm]	Δ(MLP)y ± StdDev [mm]
Timepix (no slabs)	0.004 ± 0.317	0.109 ± 0.350
Timepix in the centre of the chest slab phantom	0.199 ± 0.650	0.213 ± 0.682

4.6. Timepix in targeted alpha therapy

An autoradiography imaging study to measure radioisotope uptake in targeted alpha therapy (TAT) using the Timepix detector was performed by Al Darwish et al. (2015). Lewis Mice with Lewis lung (LL2)

tumors were treated with about 18 kBq of 227Th-labeled with the murine monoclonal antibody (DAB4) that bounds to necrotic tumor cells. The rationale is to develop α-particle-mediated bystander of nearby viable tumor cells. Finally, 5 μm tumor sections were cut from treated mice for autoradiography with Timepix. Each tumor section was mounted onto a slide with front face uncovered to allow emission of α-particles from the tumor section. Variations in tumor uptake of Th-227 labeled radioimmunoconjugate (RIC) based on the necrotic tissue volume were investigated (Darwish et al., 2015). The α-particle, photon, electron, and muon tracks were distinguished by Timepix detector in tumor section images using cluster analysis software (Turecek et al., 2011b). The results (Fig. 21) show that the uptake was four times greater when using chemotherapy before treatment with Th-227 labeled RIC (p-value of 0.026).

In another study, Timepix was used as a dosimeter in targeted alpha therapy using Ra-223 and A549 lung carcinoma cells (AL Darwish et al., 2016). This work combined Timepix dosimetry with biological dosimetry based on the γ-h2ax assay, using a Timepix-based transmission dosimetry design for α-particles (Fig. 22). A monolayer of A549 lung carcinoma cells was irradiated with an evaporated Ra-223 source positioned below the cells for ½, 1, 2 or 3 h. The Timepix detector positioned above the cells was used to determine the number of transmitted alpha particles passing through the A549 cells. Moreover, using γ-H2AX assay, DNA double-strand breaks (DSBs) were examined by fluorescence microscopy and compared for irradiated and unirradiated control cells. Approximately 20% of alpha particles were transmitted and detected by Timepix. The equivalent dose delivered to A549 cells was estimated to be approximately 0.66 Gy, 1.32 Gy, 2.53 Gy, and 3.96 Gy after ½, 1, 2 and 3 h irradiation, respectively, considering relative biological effectiveness of alpha particles of 5.5. The absorbed dose was correlated with the observed DNA DSBs, as shown in Fig. 23 (AL Darwish et al., 2016). The study confirmed that the Timepix detector could be used for transmission alpha-particle dosimetry. If cross-calibrated using biological dosimetry, this method will give a good indication of the biological effects of alpha particles.

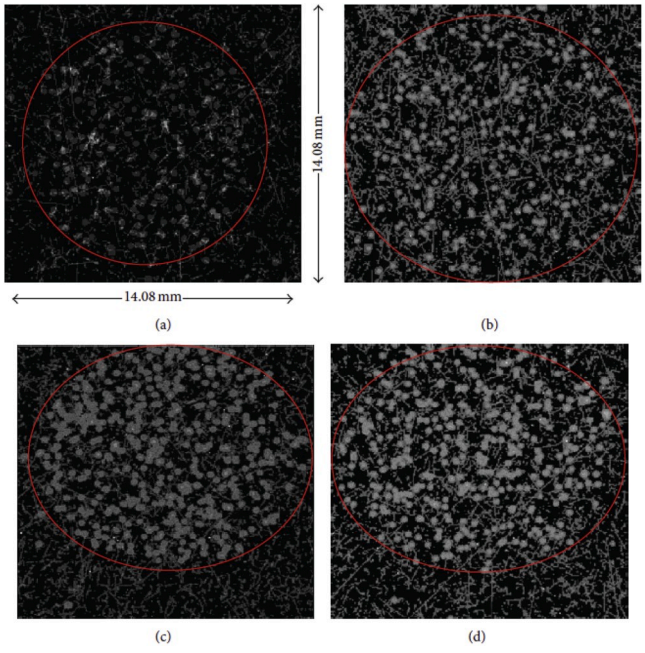

Fig. 21. Images of tumor sections from mice, (a) and (b): treated with 227Th-DAB4 alone, (c) and (d): with chemotherapy followed by 227Th-DAB4. The red circles represent the approximate tumor section boundaries, courtesy of (Darwish et al., 2015). (For interpretation of the references to color in this figure legend, the reader is referred to the Web version of this article.)

4.7. Characterization of equipment for shaping and imaging hadron mini beams

Hadron therapy has a critical advantage over conventional radiotherapy, that is a lower impact on healthy tissues in the neighborhood of a tumor that is being treated (Schardt et al., 2010b). This section discusses the feasibility of spatially fractionated hadron therapy, published in (Pugatch et al., 2017). The size and dose fields that were investigated were in the rage of 1 mm and 1×1 cm^{2,} respectively, similar to the ones studied by Martinez et al. (Martinez-Rovira et al., 2016). Monte Carlo simulations were used to optimise the hadron mini beam structures within a water phantom created by slit and matrix collimators. Simulations were used to characterize the Timepix detectors using low energy protons at the KINR Tandem generator (Kyiv) as well as high energy carbon, and oxygen ion beams at HIT (Heidelberg). Using an ideal fine pencil beam. Fig. 24 shows the Monte Carlo simulation of the dose profile delivered by protons with an energy of 105 MeV shaped by a brass collimator with five slits.

A beam of protons with an energy of 3 MeV was incident on a polyethylene target installed inside the vacuum chamber. Two Timepix detectors were positioned at 100 mm from the target center and 45° from both sides of the proton beam. The operation of the 300 μm thick silicon sensor was performed in metal mode while the other detector was operated in hybrid mode. Metal mode comprises a bare readout chip and a metal grid for collecting Secondary Emitted Electrons. In this mode, ions impinge on the surface of the Al pads which are foreseen for bump bonding ejecting secondary electrons of very low energy (~1 eV), and the ejected electrons are swept away by the electric field caused by the 20 V positive bias of the metal grid. The grid is placed 3 mm above the chip. In hybrid mode, the Timepix detector is unmodified with a 300 μm silicon micropixel sensor. Fig. 25 depicts a 2D image by a Timpix detector of the proton intensity distribution acquired in metal mode with the aluminum slit collimator installed at 3 cm in front of the Timepix detector. The pixel counts show a uniform distribution of the proton beam in each slit (Fig. 25 left). This illustrates a nice performance of the Timepix detector reflecting details of the 2D beam intensity distribution with an accuracy of 55 μm. One of the important characteristics of the multi-channel detection system is the uniformity of its response.

Studies using EBT3 gafchromic film have shown that Peak-to-Valley-Dose-Ratio (PVDR) values around ten are observed in the first few centimeters of the water phantom and decreases by a factor of approximately five at 80 mm depth. The values are comparable to studies obtained with standard X-ray beams, for which the biological effectiveness of the spatial fractionation has already been proven. Using a micropixel based detector (hybrid and metal mode) have successfully been utilized for measuring intensity distributions of the hadron mini beams in real-time. Future studies will include finer optimization of the beamline configuration and collimator system to maximize the PVDR values and provide dose distribution measurements (Pugatch et al., 2017).

5. Radiography with helium ion beams using a Timepix-based imaging system

5.1. Medical imaging with ion beams

Planning of ion beam radiotherapy treatments is based mainly on computed tomography (CT) images, which are acquired several days before the delivery of the first radiation fraction. Imaging with ion beams has a potential for improvement in terms of a direct in-vivo measurement of the integrated stopping power of the patient's tissue directly on the treatment couch, with the required precision below 1% (Poludniowski et al., 2015). This approach takes advantage of the distinct shape of the Bragg curve. The finite range of ions in matter enables gaining direct information about the integral stopping power of the imaged object if the residual energy of the ion behind the imaged object is measured.

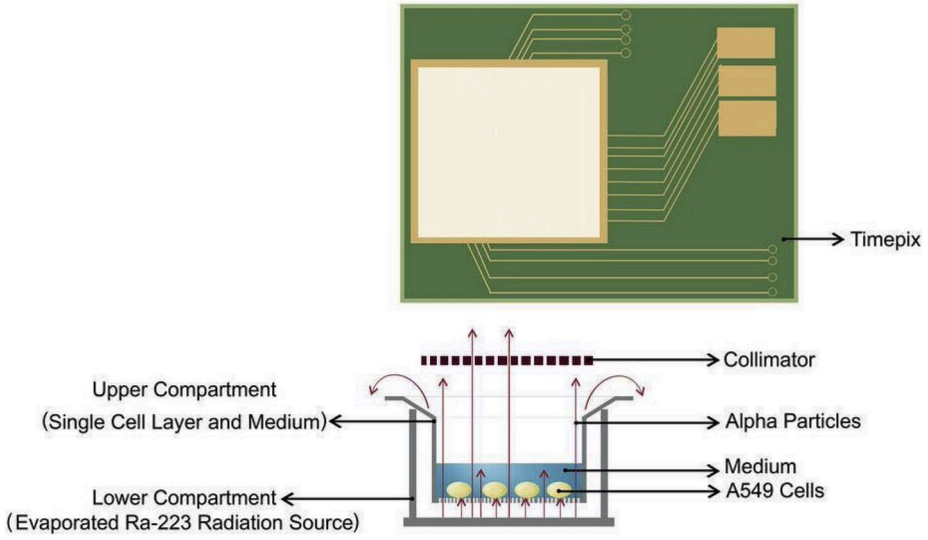

Fig. 22. Schematic diagram of the experimental setup showing the transwell system with two compartments: the lower compartment with the evaporated Ra-223 source and the upper compartment with seeded cells (cell diameter: 12.5 μm) and a thin layer of medium (approximately 45 μm height). Transmitted alpha particles are detected by Timepix, courtesy of (AL Darwish et al., 2016).

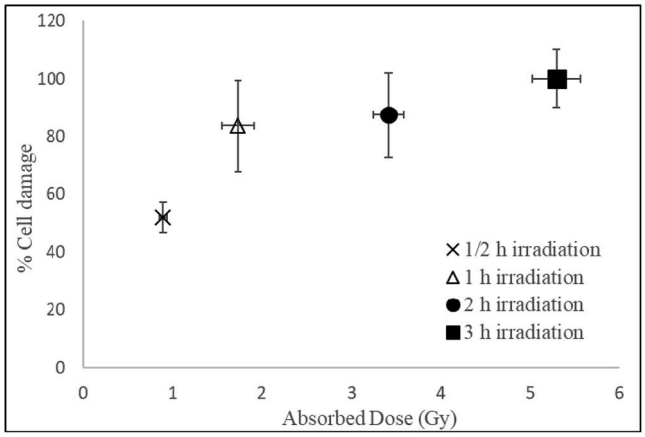

Fig. 23. Relationship between the absorbed dose to the cell layer and the media and the % of cell damage ascertained from biological dosimetry (induced by radiation and the environmental factors) after 1/2, 1, 2 and 3 h irradiation times, courtesy of (AL Darwish et al., 2016).

Moreover, the steep gradients of the Bragg peak potentially provide high sensitivity to small areal-density changes along the beam path in the imaged object. Despite nearly five decades of research, there is presently no ion imaging method which would be ready for the clinical use (Poludniowski et al., 2015). An excellent overview of ongoing and completed projects on proton beam imaging can be found in (Johnson, 2017). While the majority of the currently existing therapeutic ion beams are proton beams (Particle Therapy Cooperat, 2018), helium ions are an attractive radiation modality for both therapy and imaging. Firstly, they exhibit decreased scattering in the imaged object when compared to protons. Secondly, due to the decreased damaging potential compared to carbon ions (Gehrke et al., 2018a), the long-term effects of the high locally deposited doses, which are yet unknown, can be avoided. Being still at the beginning of the research, published investigations on helium ion imaging are currently scarce (Ohno et al., 2004; Volz et al., 2018).

5.2. Developed imaging system

At the time of development and the first tests of the reported system, there was no other fully pixelated ion imaging system published (Pugatch et al., 2017). A dedicated detection system for helium ion radiography was designed and built comprising a two-stage tracker and an energy deposition detector. All of them were composed exclusively from Timepix detectors thanks to the unique combination of their capabilities, including sufficient spatial and temporal resolution to register single therapeutic ions with a detection efficiency close to 100% and an uncertainty of the ion's hit position <55 μm, complemented by single ion's energy deposition measurements and the sensitivity to ion type. The radiographic system was composed of 5 sensitive layers (Gehrke et al., 2018a), as shown in Fig. 26. Detectors No. 1 & 2 were used as a front tracker, detectors No. 4 & 5 as a rear tracker. Layer No. 3 was used for energy deposition measurement. Optimal settings of the Timepix detectors, like the acquisition time duration and bias voltage, were found in experimental studies by maximizing the contrast-to-noise ratio (CNR) and spatial resolution (SR) of the radiographic images (Gehrke et al., 2017, 2018a).

In contrast to many single ion radiographic/tomographic systems with the image contrast based on the residual energy (or range) of the beam behind the object, the steep gradient of the energy deposition closely before the Bragg peak was exploited to gain potentially higher image contrast. The main quantity measured was the energy deposition of single ions in the sensor (material budget < 1 mm of water) of detector No.3 on a single particle basis (Gehrke et al., 2018b). For this, its response was calibrated for all 65 536 pixels (Würl, 2018). The unique positioning of the rear tracker behind the energy deposition detector enabled us to minimize the deterioration of the energy deposition information by the interactions of the ions with the tracker.

Single ion tracking was used to improve the spatial resolution of the images, which is limited by multiple Coulomb scattering of the ions in the imaged object (Gehrke et al., 2018a). The implemented two-staged tracking system enabled us to measure the trajectories of ions entering and exiting the imaged object and use them for increasing the spatial resolution. For tracking, the capability of the synchronization of all detector layers was used as a key feature of our experimental approach.

5.3. Data acquisition and processing

A dedicated data acquisition procedure and data processing algorithm was established (Gehrke et al., 2018b). It includes the identification and removal of radiation background and detector artifacts,

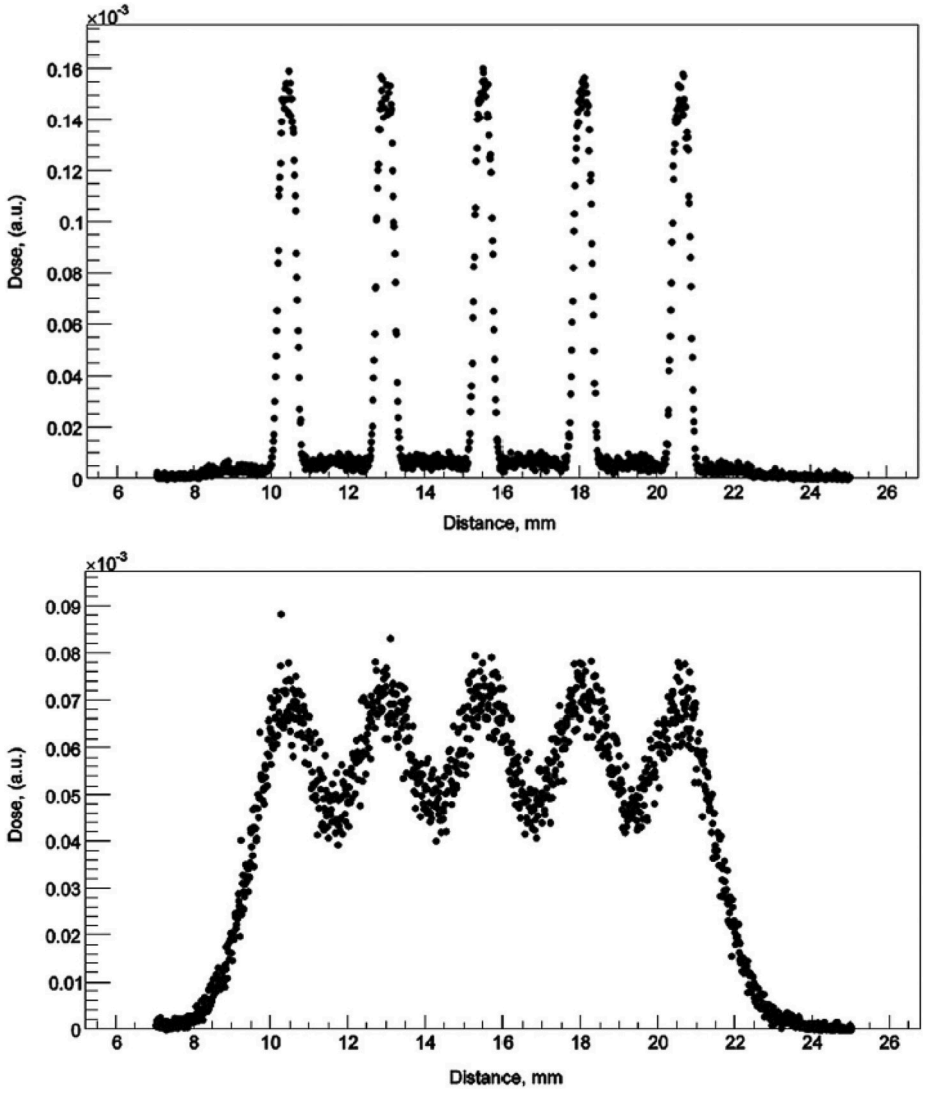

Fig. 24. Monte-Carlo simulation of the dose profile delivered by protons with an energy of 105 MeV shaped by a brass collimator with five slits (width: 0.7 mm, c-t-c distance: 2.8 mm). Top: depth in the water phantom of 1 cm. Bottom: 7 cm. Distance between phantom and collimator: 20 cm (Pugatch et al., 2017).

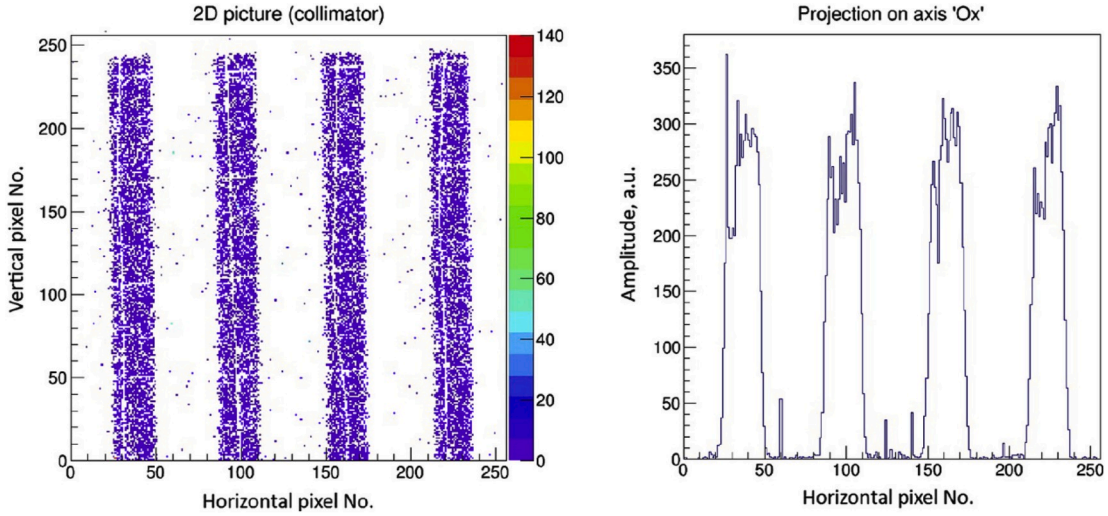

Fig. 25. Left: 2D distribution of the proton beam intensity measured by metal Timepix. Slit collimator was installed in front of the Timepix detector. Right: Projection of the data onto *X*-axis (Pugatch et al., 2017).

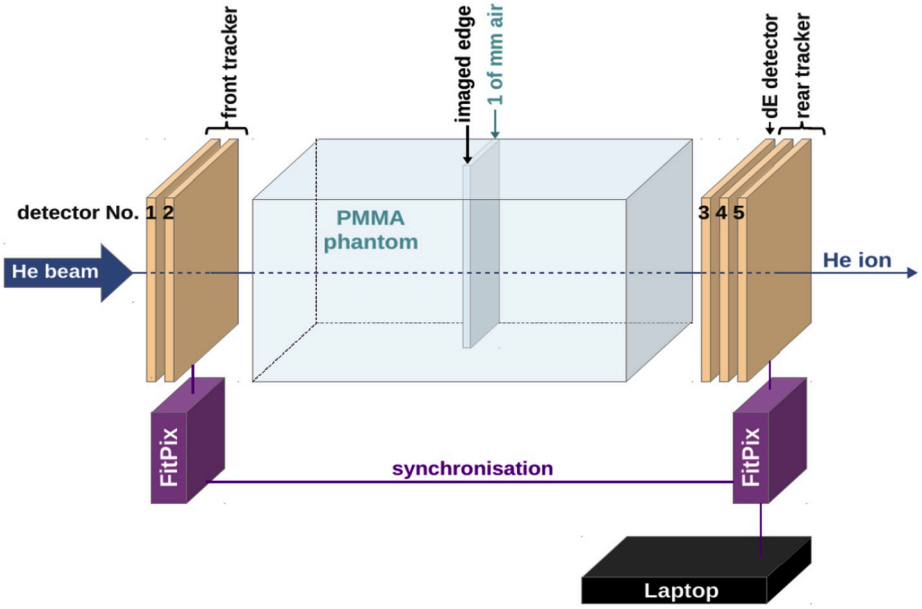

Fig. 26. A sketch of the experimental setup consisting of the front tracker, 161 mm long PMMA phantom with a 1 mm thick air inhomogeneity, energy deposition detector, and the rear tracker. Reprinted from (Martišíková et al., 2018).

homogenization of the Timepix detector response, single-ion identification, and tracking. Secondary nuclear fragments represent a challenge when ions heavier than protons are used for imaging. They have a lower charge, leading to lower energy depositions than the primary helium ions. In this way, they cause an increase in the image noise and thus decrease the CNR.

Consequently, one of the challenges was to identify and exclude hydrogen fragments from image formation. That issue was addressed by exploiting a unique single ion identification capability, which is based on pattern recognition of the signal measured in the energy deposition detector (Hartmann et al., 2017; Poludniowski et al., 2015; Arico et al., 2017). It allowed us to overcome the degradation of the images by secondary fragments of helium ions.

For accurate single-particle tracking, a precise alignment of the five detector layers, far beyond the capabilities of the laser system installed in the experimental room of the HIT facility, is crucial. A method reaching an alignment accuracy of 1 px (55 μm) was developed (Gallas et al., 2017b).

5.4. Results and discussion

The performance of the imaging method was addressed in experiments conducted at the Heidelberg Ion-Beam Therapy Facility (HIT) in Germany (Particle Therapy Cooperat, 2018). Patient-sized plastic phantoms contained clinically relevant thickness variations to be visualized (down to 0.6%) at different positions in depth. The quality of the images was evaluated quantitatively in terms of CNR and SR. The total improvement of the image quality (see Fig. 27) in terms of contrast-to-noise achieved by the described data processing method reached 350%, enabling us a clear visualization of a 0.6% thickness variation at a diagnostic X-ray dose level (Martišíková et al., 2018).

An improvement of the **spatial resolution** by 270% was reached exploiting the measured track information (Martišíková et al., 2018). The achieved spatial resolution for imaging of a 1 mm deep step at the worst-case position in a head-sized plastic phantom with helium ions was found to be 0.54 ± 0.03 lp/mm (at MTF10%) and thus 50% higher than for protons (0.37 ± 0.04 lp/mm) in the same situation (Ohno et al., 2004). This direct comparison was enabled by the applicability of the system for both ions. Fig. 28 shows an example of a helium ion beam radiography of a biological specimen – a seashell.

Using a single technology for the measurement of the energy deposition, tracking, and ion identification enabled a straight forward investigation of a different order of tracking and energy deposition modules, which is difficult, and often even impossible, with other

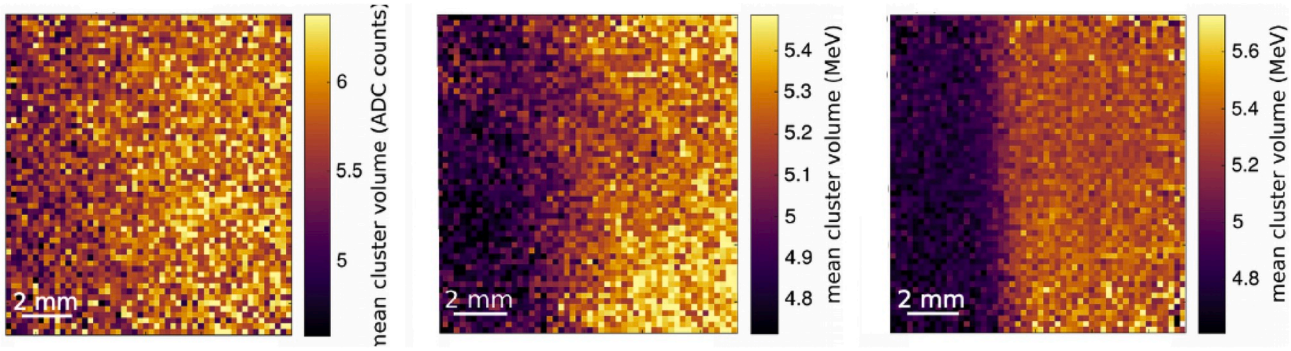

Fig. 27. A measured helium radiograph depicting a vertical air inhomogeneity (1 mm thick in the beam direction) in an otherwise homogeneous 161 mm thick PMMA phantom. The inhomogeneity was positioned in the middle of the phantom, where the lowest theoretical spatial resolution is expected. Shown are three stages of the image processing: raw data (a), image using He-ions only (b), considering measured ion directions (c). The pixel size is 220μmx220μm. Reprinted from (Martišíková et al., 2018).

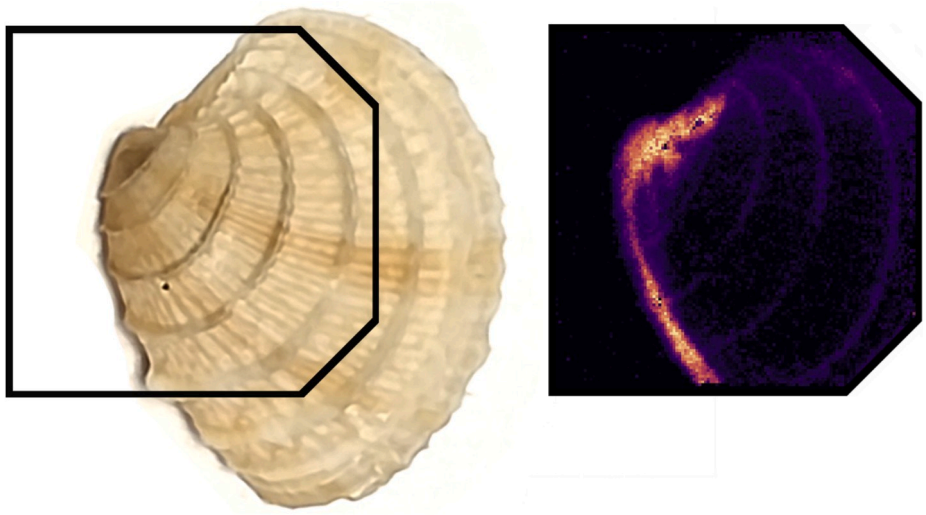

Fig. 28. Seashell (a) and its helium ion beam radiography (b). Images by Carlo Amato and Laura Ghesquire-Dierickx, German Cancer Research Center, Heidelberg, Germany (Martišíková et al., 2018).

existing ion radiography systems. In contrast to scintillating fibers or silicon strip detectors, a Timepix-based tracker provides both coordinates of a particle hit in each layer, which enables a reduction of the scattering of the ions in the imaging system. Moreover, the pixel technology allowed us to decrease the occupancy of the tracker and enabled an improved disentangling of multiple simultaneously detected particles. Based on the described results, Timepix detection technology is highly attractive for medical imaging using ion beams.

Acknowledgments

All authors value collaboration with Prague Institute of Applied Physics Prof Stanislav Pospisil and Dr Ivan Stekl. The authors would also like to acknowledge Prof Eva Bezak's valued contribution to this piece of work.

References

AL Darwish, R., Staudacher, A.H., Li, Y., Brown, M.P., Bezak, E., 2016. Development of a transmission alpha particle dosimetry technique using A549 cells and a Ra-223 source for targeted alpha therapy. Med. Phys. 43, 6145–6153.

Alderson, S.W., Lanzl, L.H., Rollins, M., Spira, L., 1962. An instrumented phantom system for analog computation of treatment plans. Am. J. Roentgenol. 87, 185–195.

Alnaghy, S., Safavi-Naeini, M., Franklin, D.R., Han, Z., Cutajar, D.L., Petasecca, M., Lerch, M., Rosenfeld, A.B., 2016. Analytical modelling and simulation of single and double cone pinholes for real-time in-body tracking of a HDR brachytherapy source. IEEE Trans. Nucl. Sci. 63 (3), 1–11.

Alnaghy, S., Cutajar, D.L., Bucci, J.A., Enari, K., Safavi-Naeini, M., Favoino, M., Tartaglia, M., Carriero, F., Jackubek, J., Pospisil, S., Lerch, M., Rosenfeld, A.B., Petasecca, M., 2017. BrachyView: combining LDR seed positions with transrectal ultrasound imaging in a prostate gel phantom. Phys. Med. 34, 55–64.

Amaldi, U., Bonomi, R., Braccini, S., Crescenti, M., Degiovanni, A., Garlasché, M., Garonna, A., Magrin, G., Mellace, C., Pearce, P., Pittà, G., Puggioni, P., Rosso, E., Verdú, S., Wegner, Andrés R., Weiss, M., Zennaro, R., 2010. Accelerators for hadrontherapy: from Lawrence cyclotrons to linacs. Nucl. Instrum. Methods Phys. Res. A 620, 563–577.

Applewhite, J., Matlaga, B., McCullough, D., Hall, M., 2001. Transrectal ultrasound and biopsy in the early diagnosis of prostate cancer. Cancer Control 8 (2).

Arico, G., Gehrke, T., Jakubek, J., Gallas, R., Berke, S., Jäkel, O., Mairani, A., Ferrari, A., Martišíková, M., 2017. Investigation of mixed ion fields in the forward direction for 220.5 MeV/u helium ion beams: comparison between water and PMMA targets. Phys. Med. Biol. 62, 8003–8024.

Ballabriga, R., Campbell, M., Llopart, X., 2007. Asic developments for radiation imaging applications: the medipix and timepix family. Nucl. Instrum. Methods Phys. Res. A 581, 485–494.

Bashkirov, V.A., Schulte, R.W., Hurley, R.F., Johnson, R.P., Sadrozinski, H.F., Zatserklyaniy, A., Plautz, T., Giacometti, V., 2016. Novel scintillation detector design and performance for proton radiography and computed tomography. Med. Phys. 43, 664–674.

Batič, M., Burger, J., Cindro, V., Kramberger, G., Mandič, I., Mikuž, M., Studen, A., Zavrtanik, M., 2010. Verification of high dose rate ir-192 source position during brachytherapy treatment. Nucl. Instrum. Methods A 617 (1–3), 206–208.

Baumann, M., Krause, M., Overgaard, J., Debus, J., Bentzen, S., Daartz, J., Richter, C., Zips, D., Bortfeld, T., 2016. Radiation oncology in the era of precision medicine. Nat. Rev. Cancer 16, 234–249.

Bisogni, M.G., Cirrone, G.A.P., Cuttone, G., Del Guerra, A., Lojacono, P., Piliero, M.A., Romano, F., Rosso, V., Sipala, V., Stefanini, A., Vecchio, S., 2008. A silicon pixel detector system as an imaging tool for proton beam characterization. In: IEEE NSS Conference Record, pp. 362–365.

Bisogni, M.G., Cirrone, G.A.P., Cuttone, G., Del Guerra, A., Lojacono, P., Piliero, M.A., Romano, F., Rosso, V., Sipala, V., Stefanini, A., 2009. Medipix2 as a tool for proton beam characterization. Nucl. Instrum. Methods 607, 48–50.

Campbell, M., Alozy, J., Ballabriga, R., Frojdh, E., Heijne, E., Llopart, X., Poikela, T., Tlustos, L., Valerio, P., Wong, W., 2016. Towards a new generation of pixel detector readout chips. J. Instrum. 11.

Cirrone, G.A.P., Cuttone, G., Lojacono, P.A., Lo Nigro, s., Mongelli, V., Patti, I.V., Privitera, G., Raffaele, L., Rifuggiato, D., Sabini, M.G., Salamone, V., Spatola, C., Valastro, L.M., 2004. A 62-MeV proton beam for the treatment of ocular melanoma at Laboratori Nazionali del Sud-INFN. IEEE Trans. Nucl. Sci. 51, 860–865.

Daido, H., Nishiuchi, M., Pirozhkov, A.S., 2012. Review of laser-driven ion sources and their applications. Rep. Prog. Phys. 75, 056401.

Darwish, R.A.L., Staudacher, A.H., Bezak, E., Brown, M.P., 2015. "Autoradiography Imaging in Targeted Alpha Therapy with Timepix Detector" Computational and Mathematical Methods in Medicine.

Dauvergne, D., Battaglia, M., Montarou, Gerard, Testa, E., 2009. New methods of real-time control imaging for ion therapy. Proc. NIRS- ETOILE Symp.

Enghardt, W., Parodi, K., Crespo, P., Fiedler, F., Pawelke, J., Pönisch, F., 2004. Dose quantification from in-beam positron emission tomography. Radiother. Oncol. 73, S96–S98.

Ferrero, V., Fiorina, E., Morrocchi, M., Pennazio, F., Baroni, G., Battistoni, G., Belcari, N., Camarlinghi, N., Ciocca, M., Guerra, A.D., Donetti, M., Giordanengo, S., Giraudo, G., Patera, V., Peroni, C., Rivetti, A., Rolo, M. Dionisio R., Rossi, S., Rosso, V., Sportelli, G., Tampellini, S., Valvo, F., Wheadon, R., Cerello, P., Bisogni, M.G., 2018. Online proton therapy monitoring: clinical test of a Silicon-photodetector-based in-beam PET. Sci. Rep. 8.

Gaa, T., Reinhart, M., Hartmann, B., Jakubek, J., Soukup, P., Jäkel, O., Martišíková, M., 2017. Visualization of air and metal inhomogeneities in phantoms irradiated by carbon ion beams using prompt secondary ions. Phys. Med. 38, 140–147.

Gallas, R., Arico, J., Burigo, L., Gehrke, T., Jakůbek, J., Granja, C., Tureček, D., Martišíková, M., 2017. A novel method for assessment of fragmentation and beam-material interactions in helium ion radiotherapy with a miniaturized setup. Phys. Med. 42, 116–126.

Gallas, R.R., Arico, G., Burigo, L.N., Gehrke, T., Jakůbek, J., Granja, C., Tureček, D., Martišíková, M., 2017. A novel method for assessment of fragmentation and beam-material interactions in helium ion radiotherapy with a miniaturized setup. Phys. Med. 42, 116–126.

Gehrke, T., Burigo, L., Arico, G., Berke, S., Jakubek, J., Turecek, D., Tessonnier, T., Mairani, A., Martišíková, M., 2017. Energy deposition measurements of single H-1, He-4 and C-12 ions of therapeutic energies in a silicon pixel detector. J. Instrum. 12, P04025.

Gehrke, T., Amato, C., Berke, S., Martišíková, M., 2018. Theoretical and experimental comparison of proton and helium-beam radiography using silicon pixel detectors. Phys. Med. Biol. 63, 035037.

Gehrke, T., Gallas, R., Jäkel, O., Martišíková, M., 2018. Proof of principle of helium-beam radiography using silicon pixel detectors for energy deposition measurement, identification, and tracking of single ions. Med. Phys. 45, 817–829.

George, S.P., Kroupa, M., Wheeler, S., Kodaira, S., Kitamura, H., Tlustos, L., Campbell-Ricketts, T., Stoffle, N.N., Semones, E., Pinsky, L., 2018. Very high energy calibration of silicon Timepix detectors. J. Instrum. 13, 11014.
Giacometti, V., Bashkirov, V.A., Piersimoni, P., Guatelli, S., Plautz, T.E., Sadrozinski, H. F., Johnson, R.P., Zatserklyaniy, A., Tessonnier, T., Parodi, K., Rosenfeld, A.B., Schulte, R.W., 2017. Software platform for simulation of a prototype proton CT scanner. Med. Phys. 44, 1002–1016.
Granja, C., Pospisil, S., 2014. Quantum dosimetry and online visualization of X-ray and charged particle radiation in aircraft at operational flight altitudes with the pixel detector timepix. Adv. Space Res. 54, 241–251.
Granja, C., Jakubek, J., Koester, U., Platkevic, M., Pospisil, S., 2011. Response of the pixel detector TimePix to heavy ions. Nucl. Instrum. Methods Phys. Res. 633, S198–S202.
Granja, C., Krist, P., Chvatil, D., Solc, J., Pospisil, S., Jakubek, J., Opalka, L., 2013. Energy loss and online directional track visualization of fast electrons with the pixel detector Timepix. Radiat. Meas. 59, 245–261.
Granja, C., Polansky, S., Vykydal, Z., Owens, A., Pospisil, S., Owens, A., Kozacek, Z., Mellab, K., Simcak, M., 2016. The SATRAM Timepix spacecraft payload in open space on board the Proba-V satellite for wide range radiation monitoring in LEO orbit. Planet. Space Sci. 125, 114–129.
Granja, C., Jakubek, J., Polansky, S., Zach, V., Krist, P., Chvatil, D., Stursa, J., Sommer, M., Ploc, O., Kodaira, S., Martisikova, M., 2018. Resolving power of pixel detector Timepix for wide-range electron, proton and ion detection. Nucl. Instrum. Methods A 908, 60–71.
Granja, C., Jakubek, J., Martisikova, M., et al., 2018. Dynamic range and resolving power of the timepix detector to heavy charged particles. J. Instrum. 13, C11003.
Granja, C., Kudela, K., Jakubek, J., et al., 2018. Directional detection of charged particles and cosmic rays with the miniaturized radiation camera MiniPIX Timepix. Nucl. Instrum. Methods Phys. Res. 911, 142–152.
Gwosch1, K., Hartmann, B., Jakubek, J., Granja, C., Soukup, P., Jäkel, O., Martišíková, M., 2013. Non-invasive monitoring of therapeutic carbon ion beams in a homogeneous phantom by tracking of secondary ions. Inst. Phys. Eng. Med. 58, 3755–3773.
Hartmann, B., Gwosch, K., Granja, C., Jakubek, J., Pospisil, S., Hikel, O., Martisikova, M., 2012. Towards fragment distinction in therapeutic carbon ion beams: a novel experimental approach using the timepix detector. In: Proc. IEEE Nucl. Sci. Symp. And Med. Imag. Conf. Record, Valencia, Spain, pp. 4076–4079.
Hartmann, B., Soukup, P., Granja, C., Jakubek, J., Pospíšil, S., Jäkel, O., Martišíková, M., 2014. Distortion of the per-pixel signal in the Timepix detector observed in high energy carbon ion beams. J. Instrum. 9, P09006.
Hartmann, B., Granja, C., Jakubek, J., Gehrke, T., Gallas, R., Pospíšil, S., Jäkel, O., Martišíková, 2017. A novel method for fragmentation studies in particle therapy: principles of ion identification". Int. J. Part. Therapy 3, 439–449.
High frame rate parallel readout interface ModuPIX-Timepix, 2015. Advacam. http://advacam.com/camera/modupix-tracker.
Jakubek, J., 2011. Precise energy calibration of pixel detector working in time-over-threshold mode. Nucl. Instrum. Methods Phys. Res. 633, S262–S266.
Jakubek, J., Granja, C., Jäkel, O., Martisikova, M., Pospisil, S., 2010. Detection and track visualization of primary and secondary radiation in hadron therapy beams with the pixel detector timepix. In: Proc. IEEE Nucl. Sci. Symp. And Med. Imag. Conf. Record, Knoxville, USA, pp. 1967–1969.
Jakubek, J., Granja, C., Hartmann, B., Jaekel, O., Martisikova, M., Opalka, L., Pospisil, S., 2011. Selective detection of secondary particles and neutrons produced in ion beam therapy with 3D sensitive voxel detector. J. Instrum. 6, C12010.
Jakubek, J., Granja, C., Hartmann, B., Jaekel, O., Martisikova, M., Opalka, L., Pospisil, S., 2011. Imaging with secondary radiation in hadron therapy beams with the 3D sensitive voxel detector. In: Proc. IEEE Nucl. Sci. Symp. And Med. Imag. Conf. Record, Valencia, Spain, pp. 2281–2284.
Johnson, R.P., 2017. Review of medical radiography and tomography with proton beams. Rep. Prog. Phys. 81, 016701.
Johnson, R.P., Bashkirov, V., DeWitt, L., Giacometti, B., Hurley, R.F., Piersimoni, P., Plautz, T.E., Sadrozinski, H.F., Schubert, K., Schulte, R., Schultze, B., Zatserklyaniy, A., 2016. A fast experimental scanner for proton CT: technical performance and first experience with phantom scans. IEEE Trans. Nucl. Sci. 63, 52–60.
Kraus, V., Holik, M., Jakubek, J., 2012. FITPix data preprocessing pipeline for the Timepix pixel detector. J. Instrum. 7, C040011.
Kroupa, M., Hoang, S., Stoffle, S., Jakubekb, J., Pinsky, L.S., 2014. Energy resolution and power consumption of Timepix detector for different detector settings and saturation of front-end electronics. J. Instrum. 9, C05008.
Martinez-Rovira, I., Brons, S., Prezado, Y., 2016. Hadron minibeam radiation therapy: feasibility study at the Heidelberg Ion-Beam Therapy Center (HIT). Radiother. Oncol. 118, S70.
Martisikova, M., Jakubek, J., Granja, C., Hartmann, B., Opálk, L., Pospíšil, S., Jäkel, O., 2011. Measurement of secondary radiation during ion beam therapy with the pixel detector Timepix. J. Instrum. 6, C11014.
Martisikova, M., Gehrke, T., Berke, S., Aricò, G., Jäkel, O., 2018. Helium ion beam imaging for image guided ion radiotherapy. Rad. Oncology 13, 109.
Martišíková, M., Gehrke, T., Berke, S., Aricò, G., Jäkel, O., 2018. Helium Ion Beam Imaging for Image Guided Ion Radiotherapy, vol. 13, p. 109.
Merchant, A.H., Newall, M., Guatelli, S., Petasecca, M., Lerch, M., Perevertaylo, V., Milluzzo, G., Petringa, G., Romano, F., Cirrone, G.A.P., Cuttone, G., Jackson, M., Rosenfeld, A.B., 2017. Feasibility study of a novel multi-strip silicon detector for use in proton therapy range verification quality assurance. Radiat. Meas. 106, 378–384.
Miniaturized Readout Interface miniPIX-Timepix, Advacam, 2016. http://advacam.com/camera/minipix.
Ohno, Y., Kohno, T., Matsufuji, N., Kanai, T., 2004. Measurement of electron density distribution using heavy ion CT. Nucl. Instrum. Methods Phys. Res. 525, 279–283.
Opalka, L., Granja, C., Hartmann, B., Jakubek, J., Jaekel, O., Martisikova, M., Pospisil, S., Solc, J., 2013. Linear energy transfer and track pattern recognition of secondary radiation generated in hadron therapy beam in a PMMA target. J. Instrum. 8, C02047.
Particle Therapy Cooperative Group, 2018. https://www.ptcog.ch/.
Penfold, S.N., Schulte, R.W., Censor, Y., Rosenfeld, A.B., 2010. Total variation superiorization schemes in proton computed tomography image reconstruction. Med. Phys. 37, 5887–5895.
Petasecca, M., Loo, K.J., Safavi-Naeini, M., Han, Z., Metcalfe, P.E., Meikle, S., Pospisil, S., Jakubek, J., Bucci, J.A., Zaider, M., Lerch, M.L.F., Qi, Y., Rosenfeld, A.B., 2013. Brachyview: proof-of-principle of a novel in-body gamma camera for low dose-rate prostate brachytherapy. Med. Phys. 40 (04), 041709.
Pinsky, L., Empl, A., Gutierrez, A., Jakubek, J., Kitamura, H., Miller, J., Leroy, C., Stoffle, N., Pospisil, S., Uchihori, Y., Yasuda, N., Zeitlin, C., 2011. Penetrating heavy ion charge and velocity discrimination with a TimePix-based Si detector (for space radiation applications). Nucl. Instrum. Methods Phys. Res. 633, S190–S193.
Poikela, T., Plosila, J., Westerlund, T., Campbell, M., De Gaspari, M., Llopart, X., Gromov, V., Kluit, R., van Beuzekom, M., Zappon, F., Zivkovic, V., Brezina, C., Desch, K., Fu, Y., Kruth, A., 2014. Timepix3: a 65K channel hybrid pixel readout chip with simultaneous ToA/ToT and sparse readout. J. Instrum. 9.
Poludniowski, G., Allinson, N.M., Evans, P.M., 2015. Proton radiography and tomography with application to proton therapy. Br. J. Radiol. 88, 20150134.
Pugatch, V., Brons, S., Campbell, M., Kovalchuk, O., Llopart, X., Martínez-Rovira, I., Momot, Ie, Okhrimenko, O., Prezado, Y., Sorokin, Yu, 2017. Nucl. Instrum. Methods Phys. Res. Sect. A Accel. Spectrom. Detect. Assoc. Equip. 872, 119–125.
Reinhardt, S., 2012. "Detection of Laser–Accelerated Protons". PhD Thesis. LMU.
Reinhart, A.M., Spindeldreier, C.K., Jakubek, J., Martišíková, M., 2017. Three dimensional reconstruction of therapeutic carbon ion beams in phantoms using single secondary ion tracks. Phys. Med. Biol. 62, 4884–4896.
Safavi-Naeini, M., Han, Z., Alnaghy, S., Cutajar, D., Petasecca, M., Lerch, M.L., Franklin, D.R., Bucci, J., Carrara, M., Zaider, M., Rosenfeld, A.B., 2015. BrachyView, a novel in-body imaging system for HDR prostate brachytherapy: experimental evaluation. Med. Phys. 42 (12), 7098–7107.
Sawakuchi, G.O., Titt, U., Mirkovic, D., Mohan, R., 2008. Density heterogeneities and the influence of multiple Coulomb and nuclear scatterings on the Bragg peak distal edge of proton therapy beams. Phys. Med. Biol. 53, 4605–4605.
Schaffner, B., Pedroni, E., 1998. The precision of proton range calculations in proton radiotherapy treatment planning: experimental verification of the relation between CT-HU and proton stopping power. Phys. Med. Biol. 43, 1579–1592.
Schardt, D., Elsässer, T., Schulz-Ertner, D., 2010. Heavy-ion tumor therapy: physical and radiobiological benefits. Rev. Mod. Phys. 82, 383–425.
Schardt, D., Elsässer, T., Schulz-Ertner, D., 2010. Heavy-ion tumor therapy: physical and radiobiological benefits. Rev. Mod. Phys. 82, 383–425.
Schulte, R., Bashkirov, V., Li, T., Liang, Z., Mueller, K., Heimann, J., Johnson, L.R., Keeney, B., Sadrozinski, H.F.W., Seiden, A., Williams, D.C., Zhang, L., Li, Z., Peggs, S., Satogata, T., Woody, C., 2004. Conceptual design of a proton computed tomography system for applications in proton radiation therapy. IEEE Trans. Nucl. Sci. 51, 866–872.
Schulte, R.W., Penfold, S.N., Tafas, J.T., Schubert, K.E., 2008. A maximum likelihood proton path formalism for application in proton computed tomography. Med. Phys. 35, 4849–4856.
Shakirin, G., Braess, H., Fiedler, F., Kunath, D., Laube, K., Parodi, K., Priegnitz, M., Enghardt, W., 2011. Implementation and workflow for PET monitoring of therapeutic ion irradiation: a comparison of in-beam, in-room, and off-line techniques. Phys. Med. Biol. 56, 1281–1298.
Shields, C.L., Shields, J.A., 2009. Ocular melanoma: relatively rare but requiring respect. Clin. Dermatol. 27, 122–133.
Soukup, P., Jakubek, J., Vykydal, Z., 2011. 3D sensitive voxel detector of ionizing radiation based on Timepix device. J. Instrum. 6, C01060.
Stoffle, N., Pinsky, L., 2018. Identification of stopping ions in a silicon Timepix detector. Nucl. Instrum. Methods Phys. Res. 880, 35–39.
Stoffle, N., Pinsky, L., Hoang, S., Idarraga, J., Kroupa, M., Jakubek, J., Turecek, D., Pospíšil, S., 2012. Initial results on charge and velocity discrimination for heavy ions using silicon-Timepix detectors". J. Instrum. 7, C12009.
Stoffle, N., Pinsky, L., Kroupa, M., Hoang, S., Idarraga, J., Amberboy, C., Rios, R., Hauss, J., Keller, J., Bahadori, A., Semones, E., Turecek, D., Jakubek, J., Vykydal, Z., Pospisil, S., 2015. Timepix-based radiation environment monitor measurements aboard the International Space Station. Nucl. Instrum. Methods Phys. Res. 782, 143–148.
Turecek, D., Jakubek, J., 2015. "PIXET Software Package Tool for Control, Readout and Online Display of Pixel Detectors Medipix/Timepix, Advacam", Prague.
Turecek, D., Pinsky, L., Jakubek, J., Vykydal, Z., Stoffle, N., Pospisil, S., 2011. Small Dosimeter based on Timepix device for international space station. J. Instrum. 6, C12037.
Turecek, D., Holy, T., Jakubek, J., Pospisil, S., Vykydal, Z., 2011. Pixelman: a multiplatform data acquisition and processing software package for Medipix2, Timepix and Medipix3 detectors. J. Instrum. 6, C01046.
Turecek, D., Holy, T., Jakubek, J., Pospisil, S., Vykydal, Z., Pixelman, ", 2011. A multi-platform data acquisition and processing software package for Medipix2, Timepix and Medipix3 detectors. J. Instrum. 6 (1), 1–8.
Volz, L., Collins-Fekete, C., Piersimoni, P., Johnson, R.P., Bashkirov, V., Schulte, R., Seco, J., 2018. Stopping power accuracy and achievable spatial resolution of helium ion imaging using a prototype particle CT detector system. Curr. Dir. Biomed. Eng. 3, 401–404.

Voulgaris, S., Nobes, J.P., Laing, R.W., Langley, S.E.M., 2008. State-of-the-art: prostate ldr brachytherap. Prostate Cancer Prostatic Dis. 11 (2), 237.
Vykydal, Z., Pospisil, S., Jakubek, J., 2006. A portable pixel detector operating as an active nuclear emulsion and its application for X-ray and neutron tomography. Proc. 9th ICATPP Conf. 779–784.
Weaver, M., Petasecca, M., Cutajar, D.L., Lerch, M.L.F., De Geronimo, G., Pinelli, D.A., Cullen, A.J., Prokopovich, D.A., Perevertaylo, V.L., Rosenfeld, A.B., Panoptes, ", 2014. Calibration of a dosimetry system for eye brachytherapy". Radiat. Meas. 71, 310–314.
Williams, D.C., 2004. The most likely path of an energetic charged particle through a uniform medium. Phys. Med. Biol. 49, 2899.
Wong, K., Erdelyi, B., Schulte, R., Bashkirov, V., Coutrakon, G., Sadrozinski, H., Penfold, S., Rosenfeld, A., 2009. The effect of tissue inhomogeneities on the accuracy of proton path reconstruction for proton computed tomography. AIP Conf. Proc. 476–482.
Würl, M., 2018. On the Spectrometry of Laser-Accelerated Particle Bunches and Laser-Driven Proton Radiography. PhD Thesis. LMU.